Bioactive Materials 44 (2025) 184–204

Contents lists available at ScienceDirect

Bioactive Materials

journal homepage: www.keaipublishing.com/en/journals/bioactive-materials

Borosilicate bioactive glass synergizing low-dose antibiotic loaded implants to combat bacteria through ATP disruption and oxidative stress to sequentially achieve osseointegration

Mengke Fan [a,b,1], Youliang Ren [c,d,1], Yanbin Zhu [a,1], Hao Zhang [b,e], Shuaijie Li [b], Chunyu Liu [b,e], Hongzhi Lv [a], Lei Chu [c], Zhiyong Hou [a], Yingze Zhang [a], Haobo Pan [b,e,**], Xu Cui [b,e,***], Wei Chen [a,*]

[a] Department of Orthopaedic Surgery the Hebei Medical University Third Hospital, Orthopaedic Research Institution of Hebei Province, NHC Key Laboratory of Intelligent Orthopaedic Equipment, Engineering Research Center of Orthopedic Minimally Invasive Intelligent Equipment of Ministry of Education, Key Laboratory of Biomechanics of Hebei Province, No.139 Ziqiang Road, Shijiazhuang, 050051, PR China

[b] Shenzhen Key Laboratory of Marine Biomedical Materials, CAS-HK Joint Lab of Biomaterials, The Key Laboratory of Biomedical Imaging Science and System, Shenzhen Institute of Advanced Technology, Chinese Academy of Sciences, Shenzhen, 518055, PR China

[c] Department of Orthopaedics, Second Affiliated Hospital of Chongqing Medical University, 76 Linjiang Road, Yuzhong Distinct, Chongqing, 400010, PR China

[d] Department of Orthopaedics, Guizhou Provincial People's Hospital, Guiyang, 550000, PR China

[e] Shenzhen Healthemes Biotechnology Co., Ltd., Shenzhen, PR China

ARTICLE INFO

Keywords:
Staphylococcus aureus
Biofilm
Osteomyelitis
Borosilicate bioactive glass
Polymethyl methacrylate

ABSTRACT

Bone infection is a catastrophe in clinical orthopedics. Despite being the standard therapy for osteomyelitis, antibiotic-loaded polymethyl methacrylate (PMMA) cement has low efficiency against bacteria in biofilms. Furthermore, high-dose antibiotic-loaded implants carry risks of bacterial resistance, tissue toxicity, and impairment of local tissue healing. By incorporating borosilicate bioactive glass (BSG) into low-dose gentamicin sulfate (GS)-loaded PMMA cement, an intelligent strategy that synergistically eradicates bacteria and sequentially promotes osseointegration, was devised. Results showed that BSG did not compromises the handling properties of the cement, but actually endowed it with an ionic and alkaline microenvironment, thereby damaging the integrity of bacterial cell walls and membranes, inhibiting ATP synthesis by disrupting the respiratory chain in cell membranes and glycogen metabolism, and elevating reactive oxygen species (ROS) levels by weakening antioxidant components (peroxisomes and carotenoids). These antibacterial characteristics of BSG synergistically reinforced the effectiveness of GS, which was far below the actual clinical dosage, achieving efficient bacterial killing and biofilm clearance by binding to the 30S subunit of ribosomes. Furthermore, the released GS and the ionic and alkaline microenvironment from the implants fostered the osteogenic activity of hBMSCs *in vitro* and coordinately enhanced osseointegration *in vivo*. Collectively, this study underscores that BSG incorporation offers a promising strategy for reducing antibiotic dosage while simultaneously enhancing the antibacterial activity and osteogenesis of implants. This approach holds potential for resolving the conflict between bacterial resistance and bone infection.

Peer review under responsibility of KeAi Communications Co., Ltd.

* Corresponding author.

** Corresponding author. Shenzhen Key Laboratory of Marine Biomedical Materials, CAS-HK Joint Lab of Biomaterials, The Key Laboratory of Biomedical Imaging Science and System, Shenzhen Institute of Advanced Technology, Chinese Academy of Sciences, Shenzhen, 518055, PR China.

*** Corresponding author. Shenzhen Key Laboratory of Marine Biomedical Materials, CAS-HK Joint Lab of Biomaterials, The Key Laboratory of Biomedical Imaging Science and System, Shenzhen Institute of Advanced Technology, Chinese Academy of Sciences, Shenzhen, 518055, PR China.

E-mail addresses: hb.pan@siat.ac.cn (H. Pan), xu.cui@siat.ac.cn (X. Cui), surgeonchenwei@126.com (W. Chen).

[1] These authors contributed equally to this work.

https://doi.org/10.1016/j.bioactmat.2024.10.009

Received 21 August 2024; Received in revised form 8 October 2024; Accepted 9 October 2024

1. Introduction

Osteomyelitis, an orthopaedical infectious disease characterized by osteolysis and bone destruction, arises from pathogenic bacteria [1–4]. It represents a catastrophic complication in clinical orthopedics and usually poses challenges to morbidity and mortality. Recent clinical epidemiological surveys have identified *Staphylococcus aureus* (*S. aureus*) as the primary pathogenic bacteria causing bone infections [4,5]. Due to the biofilm-forming potential of *S. aureus*, thus bacteria can evade detection by the immune system or antibiotics within the infection site, resulting in *S. aureus* osteomyelitis presents a high recurrence rate. Our previous report indicated that osteomyelitis induced by *S. aureus* could result in the recurrence of infections even after 29 years of treatment, and the consequent development of large infected bone defects is alarming and underscores the severity of the issue [6].

Currently, the primary approaches to treating *S. aureus* osteomyelitis involve local or systemic antibiotics and surgical intervention. Unfortunately, systemic antibiotic therapy faces difficulties due to limited drug penetration into the infected bone marrow, often necessitating prolonged courses and increased dosages, which can lead to organ toxicity and antibiotic resistance [7]. Antibiotic-loaded bone cement (ALBC) is a widely utilized systemic approach in the treatment of osteomyelitis with an infected bone defect, with the premise that high-dose local delivery is crucial for eradicating biofilm-associated bacteria [8,9]. Polymethyl methacrylate (PMMA) bone cement loaded with antibiotics stands as the most frequently utilized drug carrier for treating clinical bone infections. It is administered in various forms such as cement spacer, internal fixation, and artificial joint [9].

Despite being employed as a standardized treatment strategy for 60 years, ALBC still presents persistent limitations. These include: 1) systemic toxicity, occurring when drug distribution beyond the local site exceeds systemic clearance, leading to conditions such as acute kidney injury (AKI), 2) local tissue toxicity, 3) the ineffectiveness of commonly used antibiotics against bacteria in biofilms, 4) the emergence of drug resistance resulting from the overuse of local antibiotics [10], and 5) the low efficiency of antibiotic release in antibiotic-loaded PMMA bone cement. Furthermore, due to its lack of biological activity and osteointegration, antibiotic loaded PMMA bone cement faces dilemmas in enhancing bone cell adhesion and stimulating new bone formation, particularly in scenarios involving high concentrations of the drug. This limitation can result in the loosening of implants or joint prostheses [11]. These concerns pose significant challenges in the field of tissue engineering. Additionally, the prolonged administration of high-dose medications has sparked global alarms over bacterial drug resistance, causing a significant threat to public health globally. Addressing these issues remains imperative to safeguard public health and ensure successful orthopedic interventions [12,13].

Hence, revitalizing bioinert implants like PMMA cement with osteogenic activity under low antibiotic dosages presents an intelligent and practical strategy. This approach can synergistically combat bacteria and biofilms during the initial phase, while promoting osseointegration in the later stages. It is widely acknowledged that bioactive materials, with suitable physical and chemical properties, can be deliberately engineered and utilized to stimulate favorable cell functions, such as proliferation, differentiation, and migration, ultimately facilitating effective tissue regeneration [14]. Most impressively, certain physical and chemical properties of bioactive materials have the potential not only to eliminate biofilms but also to monitor infection recurrence over time. Furthermore, these materials can rebuild the microenvironment around implantation sites, simultaneously fulfilling the sequential requirements from anti-infection to bone regeneration and remodeling. This multifunctional capability holds great promise for revolutionizing the treatment of bone infections [15].

Bioactive glass, as a recently developed biomaterial, demonstrates satisfactory performance in various applications such as bone repair, soft tissue regeneration, and vertebral filling [16]. After being implanted in the body, bioactive glass undergoes immediate degradation, releasing ions from its network and creating an alkaline microenvironment [17–19]. Previous research has demonstrated that ion release and the alkaline microenvironment of bioactive glass represent a viable method for treating bone infections and promoting bone regeneration simultaneously [17,20–24]. This non-antibiotic antimicrobial strategy effectively mitigates the potential risk of bacterial drug resistance. Borosilicate bioactive glass (BSG) is a novel type of bioactive glass created by inserting boron into the silicate network structure to modulate the reactivity and degradation rate of bioactive glass both *in vitro* and *in vivo* [25,26]. Research has shown that adding BSG to the PMMA matrix significantly enhances osteointegration and increases bone mass and density around the implants in the lumbar vertebrae of both humans and goats. Moreover, the incorporation of BSG does not compromise the rapid solidification or high mechanical strength of the acrylic cement implants [27].

Gentamicin sulfate (GS) stands out as a frontline antibiotic extensively used in treating bone infections due to its broad spectrum, high efficacy, and stability [28]. However, despite its high concentration in PMMA, the cure rate of GS-loaded PMMA cement for bone infections can sometimes be disappointingly low. With the aim of minimizing GS loading in PMMA cement while still imparting highly efficient antibacterial and osteogenic activity, this study incorporated BSG into antibacterial PMMA cement to create a bioactive antibacterial PMMA cement. As depicted in Fig. 1, the solid phase (BSG, PMMA, GS, and ZrO2) was thoroughly mixed with the liquid phase [methyl methacrylate (MMA) (monomer) and N,N-dimethyl-p-toluidine (DMPT) (accelerator)] to produce bioactive antibacterial PMMA cement. The energy dispersive spectroscopy (EDS) mapping image demonstrated the uniform distribution of BSG within the PMMA substrate. Subsequently, the mutual promotion between the degradation microenvironment from BSG and GS release in PMMA cement synergistically produced antibacterial activity both *in vitro* and *in vivo*. RNA transcriptome sequencing (RNA-Seq) revealed that the degradation of BSG initially disrupted the integration of the cell wall and membrane of *S. aureus*. This disruption increased the membrane permeability of *S. aureus*, allowing more released ions and GS (suppressing the 30S subunit of ribosomes) to intracellularly inhibit the process of ATP synthesis and weaken antioxidant components (peroxisomes and carotenoids), triggering an oxidative stress response. The complex microenvironment, with high biocompatibility and biosafety, also synergistically facilitated the proliferation and osteogenic differentiation of hBMSCs *in vitro* and enhanced osseointegration *in vivo*. Collectively, the incorporation of BSG emerges as an effective and feasible strategy for eliminating biofilms and sequentially promoting new bone growth in the presence of a low-dose antibiotic background. This approach offers a potential solution to the challenges posed by antibiotic resistance and bone infections in clinical settings.

2. Materials and methods

2.1. Fabrication and characterization of borosilicate bioactive glass

Borosilicate bioactive glass (BSG) with composition of 6 mol%Na_2O, 8 mol.% K_2O, 8 mol.% MgO, 16 mol.% CaO, 6 mol.% SrO, 27 mol.% B_2O_3, 27 mol.% SiO_2 and 2 mol.% P_2O_5 was fabricated using a regular high temperature melting method, which was briefly described as follows. The above components were weighed according to carbonate, boric acid, silica, and phosphate (Analytical grade; China National Pharmaceutical Chemical Reagent Co., Ltd., Shanghai, China), and then placed in a 3D mixer (GH-5 L; Range Machinery Co., Ltd., Jiangyin, China) at 300 rotations/min for 30 min. The mixture was subsequently placed in a platinum crucible in a high-temperature muffle furnace at 1200 °C for 1 h. Next, the resulting high-temperature glass was poured into an ice-water mixture and quenched to form coarse BSG material. Through the processes of crushing, ball milling, and sieving, BSG with a

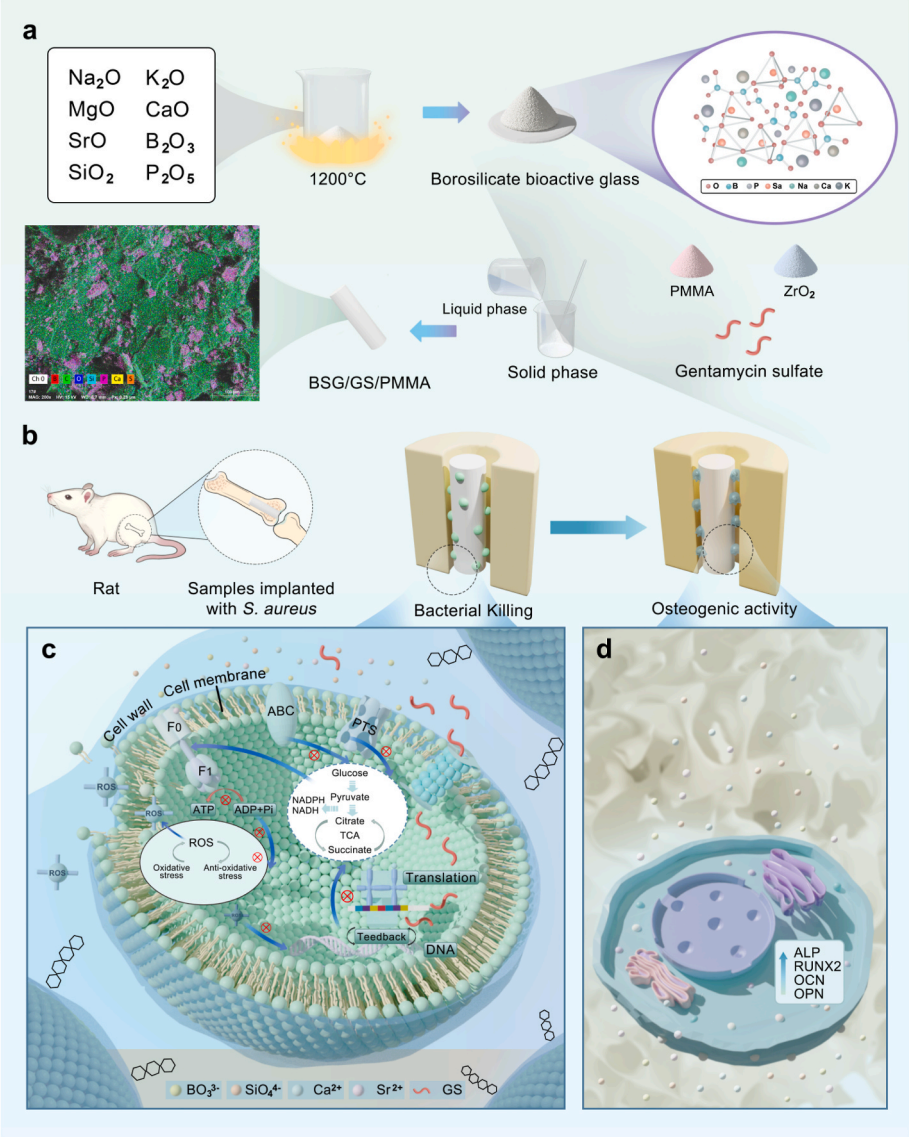

Fig. 1. Schematic illustration highlighting the preparation, application, and antibacterial mechanism of bioactive antibacterial PMMA cement. (a) Fabrication of borosilicate bioactive glass and bioactive cement. The energy dispersive spectroscopy (EDS) mapping image demonstrates the uniform distribution of BSG within the PMMA substrate. (b) After implanting the cement into the infected femoral bone marrow cavity, there is a temporal transition from combating infection to promoting bone formation. (c) The antibacterial mechanism of bioactive antibacterial PMMA cement: The diagram illustrates how ions and the alkaline microenvironment from BSG degradation disrupt bacterial cell walls and membranes, leading to intracellular ATP synthesis inhibition and ROS accumulation, ultimately resulting in bacterial eradication. (d) The osteogenic effect of bioactive antibacterial PMMA cement: This section showcases how bioactive antibacterial PMMA cement enhances osteogenesis and bone formation around the implant site.

diameter of less than 20 μm was selected. The actual composition of BSG was detected using an Inductively Coupled Plasma Spectrometer (ICP) (Optima 7000DV, PerkinElmer, Waltham, USA). The morphology of BSG was observed using Scanning Electron Microscopy (SEM, Hitachi, Japan). Fourier Transform Infrared Spectroscopy (FT-IR, Thermo Fisher Scientific, USA) and X-ray Diffraction (XRD, D8A25; Bruker, Germany) were employed to analyze the phase and composition of BSG.

2.2. Preparation and characterization of bioactive antibacterial PMMA cement

Bioactive antibacterial PMMA cement was composed of a solid phase and a setting liquid in a ratio of 2.4:1. The solid phase, which included BSG, PMMA (kindly donated by Shenzhen Healthemes Biotechnology Co., Ltd., Shenzhen, China), GS (Gentamicin sulfate, Aladdin Biochemical Technology Co., Ltd, China), and ZrO_2 (Guangdong Orient Zirconic Ind Sci & Tech Co., Ltd., Guangdong, China), was thoroughly mixed by a 3D mixer at a speed of 300 rotations/min for 30 min. The liquid components were also donated by Shenzhen Healthemes Biotechnology Co., Ltd. and consisted of methyl methacrylate (MMA) (monomer) and N,N-dimethyl-p-toluidine (DMPT) (accelerator) (Sigma-Aldrich, St. Louis, USA). The composition details were listed in Table S1. The samples were then obtained by setting the cement slurries, which were mixed from the solid and liquid components, in Teflon molds of different sizes at room temperature. The samples were then stored under room temperature conditions for 7 days and used for antibacterial and osteogenic experiments.

The distribution of BSG in bioactive antibacterial PMMA cement was observed by SEM and EDS with a mapping model that was used to detect the elements (boron, silicon, calcium, and carbon) of BSG. In short, before testing, the prepared samples of bone cement, with a diameter of 1 mm and a thickness of 3 mm, were subjected to brittle fracture, and

rough cross-sections were observed by SEM and EDS with a mapping model. Before and after being immersed in sterile polyethylene bottles containing phosphate-buffered saline (PBS, Hyclone Biotechnology Co., Ltd., China) at 37 °C for 1, 2, 4, 8, and 12 weeks, a universal testing machine (ZQ-990LA, Instrument Technology Co., Ltd., Shanghai, China) was used to test the mechanical properties of the cement, including compressive strength and four-point bending strength. According to ISO 5833:2002, the bone cement samples were 6 mm in diameter and 12 mm in thickness for compressive strength testing, and 3.3 mm in thickness, 75.0 mm in length, and 10.0 mm in width for four-point bending strength testing.

The bone cement samples, with a diameter of 10 mm and a thickness of 3 mm, were soaked in PBS in sterile polyethylene bottles for 28 days. At 1, 3, 7, 10, 14, 21, and 28 days, the soaking medium was removed and centrifuged to acquire the supernatant. Then, the pH, accumulated release of ions (BO_3^{3-}, Ca^{2+}, SiO_3^{2-}, Sr^{2+}), and accumulated release of GS were recorded using a pH meter (FiveEasyPlus™, METTLER TOLEDO, Shanghai, China), inductively coupled plasma atomic emission spectrometry (ICP, Optima 7000DV, PerkinElmer, Waltham, USA), and high-performance liquid chromatography (HPLC, 1200 type, Agilent Technologies, California, USA), respectively. The volume ratio of PBS to cement samples was calculated based on reference [29].

2.3. Antibacterial capacity of cements

2.3.1. Bacterial culture

Staphylococcus aureus (*S. aureus*, ATCC 25923), *methicillin-resistant Staphylococcus aureus* (*MRSA,* 43300), and *Escherichia coli (E.coli,* ATCC 8099*)* was cultured in sterile Luria-Bertani medium (containing 10 g/L of tryptone, 5 g/L of yeast extract, and 10 g/L of NaCl). The bacterial solution was diluted to an appropriate concentration using either physiological saline or Luria-Bertani medium prior to the experiments. The bone cement samples were irradiated with ultraviolet light for 2 h to disinfect them. 80 μL of the diluted bacterial solution (5×10^7 CFU/mL) was slowly dispensed onto the surface of the bone cement samples, which were then cultured at 37 °C in an atmospheric environment.

2.3.2. Spread plate assay

Diluted bacterial solution was inoculated onto bone cement samples (10 mm in diameter and 3 mm in thickness), and the samples were incubated at 37 °C in an atmospheric environment for 6 h. After incubation, the *S. aureus* solution was diluted 3000 times using PBS. Subsequently, 100 μL of the diluted bacterial solution was evenly spread on standard Luria-Bertani agar plates, which were then incubated at 37 °C in the ambient environment for 24 h. A fully automated colony counter (Xunshu Technology Co., Ltd., Hangzhou, China) was used for observation and image capture.

2.3.3. Bacterial viability

Diluted bacterial solution was inoculated onto bone cement samples (10 mm in diameter and 3 mm in thickness) in 24-well plates and incubated at 37 °C in an atmospheric environment for 6 h. Physiological saline (500 μL/well) containing 10 % (v/v) Alamar Blue (Solebao Biotechnology Co., Ltd., Beijing, China) was added and incubated for an additional 2 h. After incubation, 100 μL of the reactants were transferred into a 96-well plate, and the fluorescence intensity was detected using a microplate reader (ThermoFisher Scientific, USA) with an excitation wavelength of 560 nm and an emission wavelength of 590 nm. Bacterial viability was calculated as follows: (fluorescence intensity in experimental group - fluorescence intensity in the blank group)/(fluorescence intensity in the control group - fluorescence intensity in the blank group) × 100 %.

2.3.4. Bacterial live/dead staining

Diluted *S. aureus* solution was inoculated onto bone cement samples (10 mm in diameter and 3 mm in thickness), and the samples were incubated at 37 °C in an atmospheric environment for 12 h. According to the manufacturer's instructions, the bone cement samples were soaked in the blended dyes from the Live/Dead BacLight assay kit (Thermo Fisher, Massachusetts, USA) in the dark for 20 min, followed by washing twice with PBS. The pictures were taken using a confocal microscope (Leica, Hesse, Germany).

2.3.5. Bacterial morphology

Diluted *S. aureus* solution was inoculated onto bone cement samples (10 mm in diameter and 3 mm in thickness), and the samples were incubated at 37 °C in an atmospheric environment for 6 h. After incubation, the bacteria were washed three times with PBS and then fixed in 500 mL of glutaraldehyde solution (2.5 % v/v, Aladdin Biochemical Technology Co., Ltd, China) overnight. Subsequently, the bacteria were dehydrated using a gradient of ethanol (30 %, 50 %, 75 %, 90 %, 95 %, and 100 % v/v), each step lasting for 20 min, and then dried in a 60 °C environment. The bacterial morphology was observed using SEM.

2.4. Antibacterial mechanism assay

2.4.1. RNA transcriptome sequencing for S. aureus

Diluted *S. aureus* solution was inoculated onto bone cement samples (10 mm in diameter and 3 mm thickness), and incubated at 37 °C in the atmospheric environment for 6 h. After incubation, the bacterial solution was collected to extract total bacterial RNA by using a TRIzol reagent (Invitrogen, CA, USA). The RNA libraries were sequenced on the Illumina NovaseqTM 6000 platform by OE Biotech, Inc., Shanghai, China. We are grateful to OE Biotech, Inc., (Shanghai, China) for assisting in sequencing and/or bioinformatics analysis. Bioinformatic analysis was performed using the OECloud tools at https://cloud.oebiotech.com/task/. The volcano map (or other graphics) was drawn based on the R (https://www.r-project.org/) on the OECloud platform (https://cloud.oebiotech.com/task/). When $|\log_2 FC| > 1$ and P value is less than 0.05, genes are considered as differentially expressed. Gene Ontology (GO) (http://www.geneontology.org) and Kyoto Encyclopedia of Genes and Genomes (KEGG) were used to analyze differential pathways. GSEA analysis was carried out usingthe GSEA v4.2.3 tool (www.broad.mit.edu/gsea/). The connectivity between protein pathways was analyzed by a protein-protein interaction (PPI) network diagram.

2.4.2. Bacterial membrane permeability

Diluted *S. aureus* solution was inoculated onto bone cement samples (10 mm in diameter and 3 mm in thickness), and incubated at 37 °C in an atmospheric environment for 6 h. The bacterial protein leakage was determined using the Micro BCA protein assay reagent kit (Thermo Fisher, Massachusetts, USA). Following the standard procedure, the collected bacterial solution was centrifuged at 6000 rpm for 5 min. The absorbance of the supernatant was measured at 562 nm, and subsequently, the protein concentrations were calculated. o-Nitrophenyl β-D-galactopyranoside (ONPG) was used to further detect membrane permeability. ONPG is hydrolyzed into galactose and yellow o-nitrophenol. The absorbance of o-nitrophenol can be detected at 420 nm. After the initial 6-h incubation, ONPG was added and the samples were incubated at 37 °C for an additional 30 min. Finally, the absorbance was measured using a microplate reader.

2.4.3. Biofilm formation

Crystal violet staining is a commonly used method to visualize bacterial biofilms. After incubation, 500 μL of methanol was added to fix the biofilms for 15 min. Methanol was removed by air-drying. Finally, the bone cement samples were stained with 0.1 % crystal violet solution for 15 min. Subsequently, the bacterial biofilms were dissolved in 95 % ethanol for 30 min. The absorbance of the resulting solution was measured at 595 nm using a microplate reader.

2.4.4. Detection of ATP

According to the ATP detection kit (Solebao Biotechnology Co., Ltd., Beijing, China), bacteria were collected after incubation and diluted with PBS to a total volume of 500 μL. Ultrasonic crushing was performed (ice bath, power 200W, ultrasonic for 2 s, stop for 1 s, total time 1 min). Then, the samples were centrifuged at 4 °C at 10,000 g for 10 min. The supernatant was transferred to new Eppendorf tubes, and 500 μL of chloroform was added to each tube. The tubes were thoroughly shaken and mixed. Subsequently, the samples were centrifuged again at 4 °C at 10,000 g for 3 min. The absorbance of the supernatant was measured at 340 nm using a microplate reader.

2.4.5. Detection of ROS

According to the ROS detection kit (Solebao Biotechnology Co., Ltd., Beijing, China), 500 μL of dichlorodihydrofluorescein diacetate (DCFH-DA) (10 mM, diluted 1:1000 with PBS; Beyotime Biotechnology Co., Ltd, Shanghai, China) was added to the samples and incubated at 37 °C in an atmospheric environment for 30 min. After incubation, the green fluorescence of ROS was observed using an inverted fluorescence microscope (Olympus Optical Technology, Japan). The fluorescence intensity was then measured using a Microplate reader at an excitation wavelength of 480 nm and an emission wavelength of 525 nm.

2.5. Osteogenic differentiation of hBMSCs

2.5.1. Cell culture

Human bone marrow mesenchymal stem cells (hBMSCs) were purchased from the American Type Culture Collection (ATCC, Virginia, USA) and were cultured in a medium consisting of α-MEM (Gibco, USA) supplemented with 10 % fetal bovine serum (FBS, Gibco, USA) and 1 % penicillin/streptomycin (P/S, Hyclone Biotechnology Co., Ltd., China). The cells were maintained at 37 °C in a 5 % CO_2 incubator. Prior to the start of the experiment, all bone cement samples were irradiated with ultraviolet light for 2 h.

2.5.2. Cellular compatibility and proliferation

hBMSCs (3.5×10^4 cells/well) were added onto bone cement samples (10 mm in diameter and 3 mm in thickness) in 48-well plates and incubated at 37 °C in a 5 % CO_2 environment. The Cell Counting Kit-8 (CCK-8) reagent (1:9, Beyotime Biotechnology Co., Ltd, Shanghai, China) was added at 1 day, 3 days, and 5 days, respectively, and the plates were further incubated at 37 °C in a 5 % CO_2 environment for 2 h. The absorbance of the reaction solution was measured at 450 nm using a microplate reader.

2.5.3. Live/dead staining

hBMSCs (3.5×10^5 cells/well) were added to bone cement samples (10 mm in diameter and 3 mm in thickness) in 12-well plates and incubated at 37 °C in a 5 % CO_2 environment for 24 h. According to the Live/Dead staining kit (Beyotime Biotechnology Co., Ltd, Shanghai, China), and pre-mixed live/dead staining reagents (calcein and propidium) 300 μL were added. After 15 min, bone cement samples were observed and taken pictures using an inverted fluorescence microscope.

2.5.4. Cellular morphology

hBMSCs (3.5×10^5 cells/well) were added to bone cement samples (10 mm in diameter and 3 mm thickness) in 12-well plates and incubated at 37 °C in a 5 % CO_2 environment for 24 h. Then, 500 μL of 4 % paraformaldehyde was added to fix the cells for 30 min. Subsequently, 300 μL of 0.1 % Triton X-100 (Sigma-Aldrich, St Louis, USA) was added to increase cell membrane permeability. After that, 300 μL of Actin Tracker Red-594 (1:500, Beyotime Biotechnology Co., Ltd, Shanghai, China) was added to stain the cytoskeleton actin for 15 min, followed by staining the cell nucleus with DAPI (4' 6-diamino-2-phenylindole dihydrochloride) (1:5000, Beyotime Biotechnology Co., Ltd, Shanghai, China) for 10 min. Finally, the samples were observed and photographed using an inverted fluorescence microscope.

2.5.5. Osteogenic differentiation

The osteoblastic differentiation of hBMSCs was evaluated by alkaline phosphatase (ALP) staining and Alizarin Red S (ARS) staining. hBMSCs (3.5×10^5 cells/well) were added to bone cement samples (10 mm in diameter and 3 mm in thickness) in 12-well plates and incubated at 37 °C in a 5 % CO_2 environment. When the confluence of hBMSCs reached 80 % or more, the bone cement samples were transferred to the upper chamber and cultured with 2 mL of osteogenesis-inducing medium containing β-glycerol phosphate (10 mM), L-ascorbic acid (50 μM), and dexamethasone (0.1 μM). On the 7th day, 500 μL of 4 % paraformaldehyde was added to fix the cells for 20 min. According to the ALP assay kit instructions (Beyotime Biotechnology Co., Ltd, Shanghai, China), 300 μL of the mixture was added, and the samples were incubated at room temperature for 12 h. On the 14th day, after fixing the cells, 300 μL of 2 % ARS working solution (Sigma Aldrich, St. Louis, USA) was added for 15 min. All samples were observed and photographed under an inverted microscope. Subsequently, cetylpyridine chloride solution (Aladdin Biochemical Technology Co., Ltd, China) was added, and the samples were incubated at room temperature in the dark for 30 min. Finally, the absorbance of the mixture was measured at 562 nm using a microplate reader.

2.5.6. qRT-PCR

According to the instructions of the mRNA extraction kit (Magen Biotechnology Co., Ltd, China), the total RNA was extracted from osteoblasts and then reverse transcribed into cDNA using the PrimeScript RT reagent kit (20 μL). Reverse transcription polymerase chain reaction (qRT-PCR) was employed to detect the expression of osteogenic-related genes in hBMSCs, including *ALP* (at 7 days), *RUNX2* (at 7 days), *OCN* (at 14 days), and *OPN* (at 14 days). GAPDH was used as the reference gene. The primer sequences used for the genes are presented in Table S2.

2.5.7. Western blot

The cells were lysed using RIPA lysis solution containing the protease inhibitor PMSF (Beyotime Biotechnology Co., Ltd, Shanghai, China). The BCA protein quantification kit (Thermo Fisher Scientific, USA) was used to determine the concentration of total protein. According to the SDS-PAGE gel kit instructions (Vazyme Biotechnology Co., Ltd, China), the proteins were separated using a voltage of 110V. Then, the protein was transferred to a polyvinylidene fluoride (PVDF) membrane (Sigma Aldrich, St. Louis, USA) using a constant current of 300 mA. The PVDF membrane was blocked with 5 % milk (Sigma-Aldrich, St. Louis, USA) at room temperature for 1.5 h. The membrane was then incubated with anti-RUNX2 (1:1000, Abcam, ab23981, Cambridge, UK) and anti-OCN (1:1000, Abcam, ab133612, Cambridge, UK) antibodies at 4 °C overnight. The next day, the membrane was washed with TBST and incubated with the secondary antibody at room temperature for 1 h. The blots were detected using a chemiluminescence kit (Sigma Aldrich, St. Louis, USA). Semi-quantitative analysis was performed using Image J software (National Institutes of Health, USA).

2.6. Animal experiment

2.6.1. Establishment of rat femoral bone marrow infection model

All animal experiments were approved by the Animal Ethics Committee of Shenzhen Institute of Advanced Technology, Chinese Academy of Sciences (Approval number: YSY-DWLL-2021016) and conducted in accordance with the National Laboratory Animal Care and Use Guidelines. Thirty-two male SD rats weighing 350–400 g were purchased from Weitong Lihua Biotechnology Co., Ltd. (China). These rats were divided into four groups (n = 8): the pure PMMA (abbreviated as PMMA), 1 wt% GS/PMMA (abbreviated as G/PMMA), 30 wt% BSG/PMMA (abbreviated as B/PMMA) and 30 wt% BSG/1 wt% GS/PMMA (abbreviated as B/G/PMMA). All rats were fed similarly. The anti-infection ability of bone

cement implants was observed in the first two weeks, and both anti-infection ability and osteogenic capacity were evaluated at 4 and 8 weeks.

A cylindrical rubber mold with an inner diameter of 1.2 mm was used to create bone cement implants. After solidifying for 24 h, the implants were trimmed to 10 mm using sterile scissors. Prior to surgery, all bone cement implants were irradiated with ultraviolet light for 2 h. All SD rats underwent lower limb skin preparation and disinfection. A small animal anesthesia machine (RWD, China) with isoflurane (RWD, China) was used for continuous inhalation anesthesia. A 2 cm incision was made on the anterior lateral side of the knee joint, and the muscles and tendons were bluntly separated. The patella was pulled inward to cause patellar dislocation. A 1.5 mm Kirschner wire was used to drill holes in the femoral trochlea until the bone marrow cavity was reached. The bone fragments were rinsed with normal saline. Before implantation, all cement implants were contaminated in a diluted *S. aureus* solution (5×10^7 CFU/mL) in an Eppendorf tube for 5 s. The implants contaminated with *S. aureus* were then immediately inserted into the bone marrow cavity, followed by sealing with bone wax. The incision was rinsed, sutured, and dressed. SD rats were euthanized, and samples were collected after 1, 2, 4, and 8 weeks.

2.6.2. Antibacterial vitality in vivo

To assess the antibacterial effectiveness of bioactive antibacterial PMMA cement, the implants were removed after 1 week and 2 weeks, respectively. One week after the implantation surgery, the infected femoral area was measured using X-ray equipment (SCANCO MidicecAG, VivaCT40), and radiographic scores were calculated. The implants were then removed, rolled on a standard agar plate, and placed into a sample bottle (105 mm × 27.5 mm; Junlibo Biotechnology Co., Ltd., Beijing, China) containing 30 mL of Luria-Bertani medium. These were incubated at 37 °C in an atmospheric environment for 24 h. Pictures were taken using a fully automatic colony counter. At 2 weeks post-implantation surgery, the femoral area was measured again using X-ray equipment. The implants were removed and decalcified with a 12 % EDTA solution for 4 weeks. After embedding in paraffin, tissue sections of 5 μm thickness were prepared. The paraffin slices were placed in a 55 °C oven overnight, then dewaxed in a series of solvents (xylene, 100 % alcohol, 95 % alcohol, 90 % alcohol, 85 % alcohol, 70 % alcohol). H&E staining, Gram staining, and Masson's trichrome staining were performed to evaluate the impact of bacteria on bone. An inverted fluorescence microscope was used to analyze the histopathological microtomography.

2.6.3. Osseointegration

At 4 weeks and 8 weeks after the implantation surgery, femur samples were collected for Micro-computed tomography (Micro-CT) scanning (SCANCO Medical AG, VivaCT40) to conduct tomography analysis. The region of interest (ROI) for the Micro-CT had a height of 10.0 mm and a diameter of 1.5 mm. A 3D reconstruction was performed to quantitatively measure bone parameters, such as bone volume/total volume (BV/TV), trabecular thickness (Tb.Th), and the number of trabeculae (Tb.N). Following the 3D analysis, the implants were decalcified using a 12 % ethylenediaminetetraacetic acid (EDTA) solution. Subsequently, they were embedded in paraffin, and 5 μm thick sections were prepared. The paraffin sections were then incubated in a 55 °C oven overnight. After incubation, the sections were dewaxed using a series of solvents (xylene, 100 % alcohol, 95 % alcohol, 90 % alcohol, 85 % alcohol, 70 % alcohol). H&E staining, Masson staining, and Safranin O-Fast Green staining were conducted to evaluate the newly formed bone around the bone cement implants. An inverted fluorescence microscope was used to analyze the histopathological sections.

2.6.4. Biocompatibility in vivo

The biocompatibility of bone cements was evaluated using pathological sections. One week and two weeks after the implantation surgery, the major internal organs, including the heart, liver, spleen, lungs, and kidneys, were collected. H&E staining was employed to assess pathological changes in these organs and identify any toxic reactions.

2.7. Statistical analysis

All statistical significance was analyzed using GraphPad Prism 9.0 software. Data are presented as means ± SD. Differences between the two groups were analyzed by the independent samples Student's t-test. Differences among the four groups were analyzed by one-way ANOVA with Tukey's post hoc test as described in the figure legends. Values of $^{*}P < 0.05$, $^{**}P < 0.01$, $^{***}P < 0.001$ were considered statistically significant. Values of $^{ns}P > 0.05$ were considered not statistically significant.

3. Results

3.1. Fabrication and characterization of bioactive antibacterial PMMA cement

Based on previously reported protocols, borosilicate bioactive glass (BSG) with a composition of 6 mol.% Na_2O, 8 mol.% K_2O, 8 mol.% MgO, 16 mol.% CaO, 6 mol.% SrO, 27 mol.% B_2O_3, 27 mol.% SiO_2, and 2 mol.% P_2O_5 was fabricated using the melting method [27]. A symmetric comparison by inductively coupled plasma spectrometry (ICP) testing revealed no significant difference between the designed and actual composition (Table S3). Scanning electron microscope (SEM) images demonstrated that BSG exhibited a typical irregular particle morphology with a particle size of <20 μm (Fig. 2a). Fourier transform infrared (FT-IR) spectroscopy detected two wide vibrational bands around 440-540 cm^{-1} and 994-1075 cm^{-1}, corresponding to bending vibration and asymmetric stretching vibration of Si-O-Si, respectively. The band near 1400 cm^{-1} was attributed to the stretching vibration of B-O-B in the boron oxygen tetrahedron [BO4], and the band near 600 cm-1 was due to the O-P-O bending vibration (Fig. S1a). As shown in Fig. S1b, X-ray diffraction (XRD) analysis data displayed a broad diffuse diffraction peak around 30°, indicating the amorphous state of the BSG particles. These results demonstrate that BSG with a dual network of boron-oxygen and silicon-oxygen was successfully synthesized.

BSG was incorporated into antibacterial PMMA cement to assess its synergistic antibacterial effects against the typical Gram-positive bacterial model, *Staphylococcus aureus* (*S. aureus*). Detailed information regarding the cement compositions is provided in Table S1. In this study, two specific amounts of BSG (10 wt% and 30 wt%, based on the weight of the solid phase) were introduced into PMMA cement, following our previous research [27]. After solidification, the samples were placed at room temperature for 1 week. The surfaces of cement disks (10 mm in diameter and 3 mm in thickness) were cultured with *S. aureus* (5×10^7 CFU/mL) for 6 h, and bacterial viability was assessed using the cell counting kit-8 (CCK-8) method.

Initially, pure PMMA cement was evaluated for its antibacterial activity. No significant inhibition of *S. aureus* was observed (Fig. S2). Subsequently, PMMA cement with various GS loadings (named as antibacterial PMMA cement) was assessed. The antibacterial rates for 0.1 wt% GS/PMMA, 1 wt% GS/PMMA, 3 wt% GS/PMMA, 5 wt% GS/PMMA, and 10 wt% GS/PMMA were 45.3 % ± 2.0 %, 54.7 % ± 1.8 %, 60.6 % ± 2.3 %, 67.3 % ± 1.4 %, and 68.5 % ± 1.2 %, respectively. Analysis of these results for antibacterial PMMA cement reveals that within a certain range (from 0.1 wt% GS to 10 wt% GS), an increase in GS dosage gradually enhances the antibacterial ability of the cement. Significant differences ($P < 0.05$) in antibacterial ability were only observed between cements of 0.1 wt% GS/PMMA and 1 wt% GS/PMMA. However, a further increase in GS loading in PMMA cement did not significantly enhance the antibacterial rate of the cements (Fig. S2).

For PMMA cement with only BSG incorporation (referred to as bioactive PMMA cement), the suppression of *S. aureus* was also

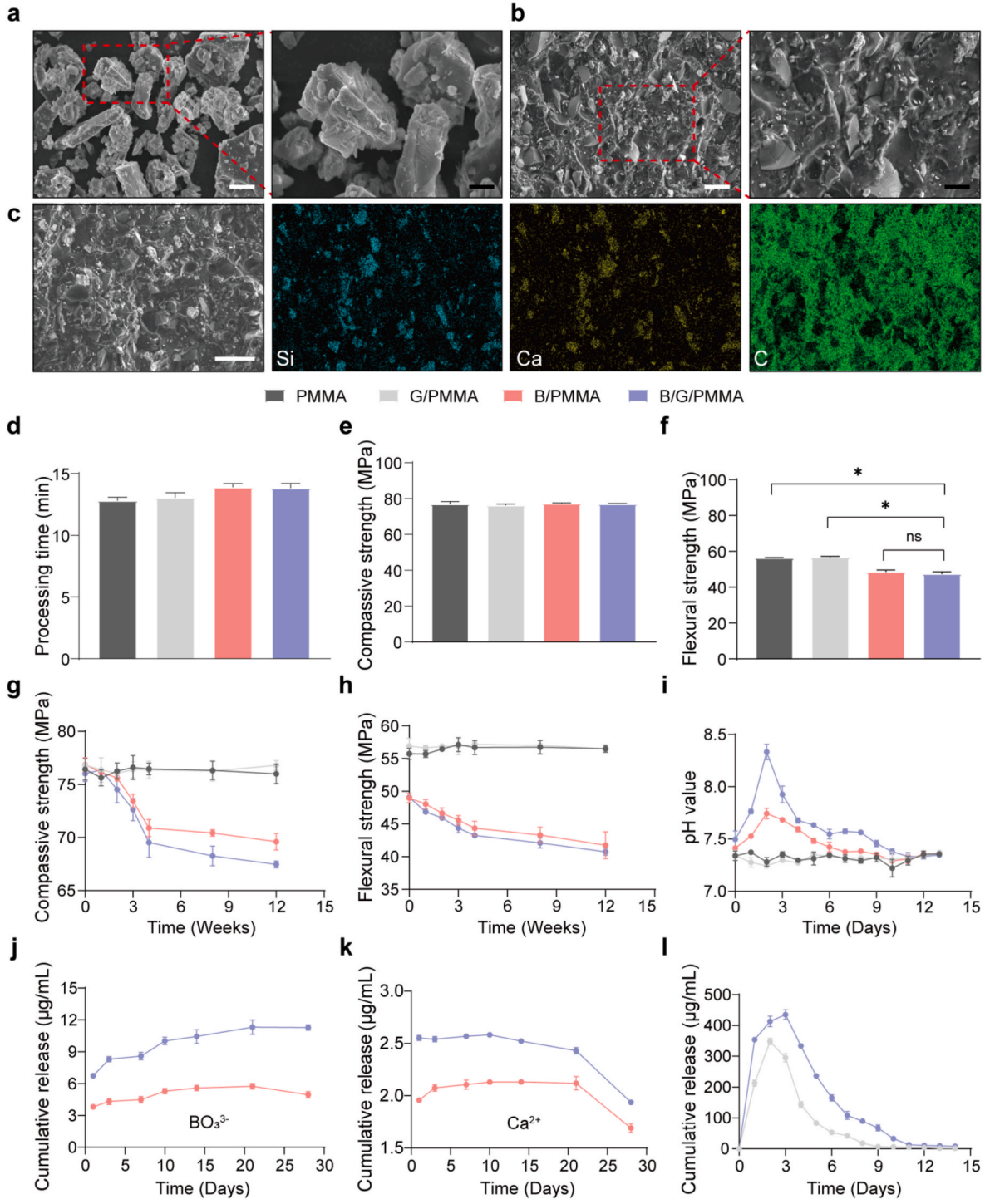

Fig. 2. Fabrication and characterization of bioactive antibacterial PMMA cement. (a) Scanning electron microscope (SEM) images of BSG particles (white scale bar = 5 μm; black scale bar = 2 μm). (b) Cross-section of the morphology of B/G/PMMA cement (white scale bar = 50 μm; black scale bar = 20 μm) and (c) elemental energy-dispersive X-ray spectroscopy (EDS) mapping of B/G/PMMA cement (scale bar = 100 μm). (d) Processing times of cements. (e) Compressive strength and (f) four-point bending strength of pre-cured cements. Changes in compressive strength (g) and four-point bending strength (h) after cements were immersed in PBS. (i) pH value, (j) cumulative release of BO_3^{3-}, (k) cumulative release of Ca^{2+}, and (l) cumulative release of gentamicin sulfate (GS) of cements in PBS. Data are presented as means ± SD. Error bars represent the standard deviation (n = 3). P values were calculated by one-way ANOVA with Tukey's post hoc test and Student's t-test; $^{ns}P > 0.05$, $^{*}P < 0.05$.

confirmed in Fig. S2. Importantly, higher amounts of BSG incorporation resulted in better antibacterial activity. The antibacterial rate of the 30 wt% BSG/PMMA cement (64.9 % ± 3.7 %) was significantly higher than that of the 10 wt% BSG/PMMA cement (33.7 % ± 2.9 %). The positive correlation between the antibacterial activity of BSG and its proportion in the PMMA cement is consistent with previous reports on the clinical outcomes of bioactive glass in bone infections [20–22]. Additionally, it is worth noting that a recommended dosage of 10 wt% GS loading in PMMA cement is commonly used by clinicians for implant-related bone infections. The comparable antibacterial rate of 30 wt% BSG/PMMA

cement to that of 5 wt% and 10 wt% GS/PMMA cements reveals the relatively satisfactory inhibition achieved by bioactive PMMA cement with 30 wt% BSG.

To further investigate the potential synergistic antibacterial activity between BSG and low-dose GS loading in PMMA cement, two specific formulations of PMMA cements were selected. Our results demonstrated that the antibacterial rate for 30 wt% BSG/0.1 wt% GS/PMMA cement was 75.4 % ± 0.7 %, even higher than those of 5 wt% GS/PMMA and 10 wt% GS/PMMA cements. Furthermore, the 30 wt% BSG/1 wt% GS/PMMA cement displayed optimal antibacterial activity, with an antibacterial rate of 84.9 % ± 2.2 % (Fig. S2). Previous reports have recommended that, to achieve reliable treatment efficacy for periprosthetic joint infections (PJI), the loading of antibiotics into PMMA cement should be no less than 3.6 g per 40 g of PMMA cement, and this recommendation still serves as the conventional standard for orthopedic surgeons [30]. Obviously, the recommended antibiotic loading dosage is much higher than the GS concentration in the bioactive antibacterial PMMA cement presented in this paper, which suggests that 30 wt% BSG/1 wt% GS/PMMA cement exhibits a promising potential for synergistic bacterial inhibition, or even in avoiding the development of drug resistance in bacteria.

Based on the aforementioned research, we decided to choose cements of pure PMMA (abbreviated as PMMA), 1 wt% GS/PMMA (abbreviated as G/PMMA), 30 wt% BSG/PMMA (abbreviated as B/PMMA), and 30 wt% BSG/1 wt% GS/PMMA (abbreviated as B/G/PMMA) (Table S4), to systematically explore their antibacterial activity against *S. aureus* and osteogenic activity, both *in vitro* and *in vivo*. Additionally, we will further conduct investigations into the mechanisms underlying how BSG synergistically enhances the antibacterial activity of low-dose drug-loaded PMMA cement against *S. aureus*.

It is essential to thoroughly assess whether the incorporation of BSG affects the clinical performance of PMMA cements. Generally, after the solid phase and setting liquid of PMMA cement are mixed, free radical polymerization of methyl methacrylate (MMA) into PMMA is immediately triggered by the accelerator, leading to a significant release of heat that can cause considerable damage to the tissue surrounding implants. In our results, the B/PMMA and B/G/PMMA groups exhibited slightly lower temperatures compared to the other groups throughout the entire solidification process (Fig. S3a). Subsequently, the distribution of BSG in the cement was observed. SEM images demonstrated that irregular BSG particles are uniformly distributed within the PMMA matrix in B/G/PMMA cement (Fig. 2b). Energy dispersive spectroscopy (EDS) mapping further displayed uniformly distributed Si (blue) and Ca (yellow) in the green PMMA matrix (Fig. 2c). The uniform distribution of BSG within the PMMA matrix could create connective micropores upon BSG degradation, which may facilitate the formation of an osteointegration interface between the cement and host bone.

Under a simulated clinical application scenario with a temperature range of 22 °C–24 °C and humidity of 55 %–60 %, the processing time of bioactive antibacterial PMMA cement, including mixing time, waiting time, application time, and setting time of the cement paste, was analyzed to evaluate the practicality of minimally invasive administration (Fig. 2d). The recommended mixing time for B/G/PMMA was found to be 1.5 min, and then the homogeneous paste should be transferred into a syringe immediately. After a 3-min waiting period, the B/G/PMMA cement paste reaches the appropriate consistency for smooth injection. The application time, defined as the duration from starting to extrude until the cement paste can no longer be injected, was 6 min and 31 s. After the application time, there is a 4-min setting time (totaling 14 min). The processing times in the PMMA group, G/PMMA group, and B/PMMA group were 12.4, 12.8, and 13.9 min, respectively (Table S5). These time scales not only meet the international standard for surgical implants-acrylic resin cements (ISO 5833:2002) (no longer than 15 min), but also provide orthopedists with sufficient manipulation time to effectively apply the cement paste in clinical settings [31].

Meanwhile, mechanical properties, including compressive strength, four-point bending strength, and the relevant flexural modulus of precured cements, were also investigated according to ISO 5833:2002. As shown in Fig. 2e, the compressive strengths of cement samples were (76.7 ± 1.0) MPa for the PMMA group, (76.6 ± 0.9) MPa for the G/PMMA group, (75.3 ± 0.9) MPa for the B/PMMA group, and (75.4 ± 0.9) MPa for the B/G/PMMA group, respectively. These values exceeded the minimum requirement of 70 MPa set by the international standard. As for four-point bending strengths, they were (56.2 ± 0.4) MPa for the PMMA group, (56.6 ± 0.6) MPa for the G/PMMA group, (48.4 ± 1.2) MPa for the B/PMMA group, and (47.4 ± 1.2) MPa for the B/G/PMMA group, respectively (Fig. 2f). Unfortunately, a slight reduction in four-point bending strengths was observed for the B/PMMA and B/G/PMMA groups, with these values falling just below the 50 MPa requirement specified in ISO 5833:2002. Upon immersion in PBS, both compressive strengths and four-point bending strengths of the B/PMMA and B/G/PMMA groups decreased with increasing immersion time (Fig. 2g and h). However, for the PMMA and G/PMMA groups, there was only a marginal decrease in compressive strengths and four-point bending strengths after 12 weeks of immersion in PBS. After 12 weeks, the compressive strength of the B/PMMA and B/G/PMMA groups decreased from (76.9 ± 0.7) MPa to (69.6 ± 0.8) MPa, and from (76.0 ± 0.7) MPa to (67.5 ± 0.3) MPa, respectively (Fig. 2g). Similarly, the four-point bending strengths for the B/PMMA and B/G/PMMA groups decreased from (48.9 ± 0.7) MPa to (41.7 ± 2.1) MPa, and from (49.1 ± 0.3) MPa to (40.7 ± 0.6) MPa, respectively, after 12 weeks (Fig. 2h). Our previous research also indicated a decrease in the mechanical performance of BSG-incorporated PMMA cements, which could be attributed to the increase in micropores within the PMMA substrate resulting from BSG degradation [27]. In the osteoporotic microenvironment, this degradation-induced performance can narrow the stiffness mismatch between implants and host bone, which, paradoxically, may prevent the occurrence of adjacent vertebral fractures.

In summarizing the characterization of the prepared cements in this study, it can be concluded that the incorporation of BSG or drug-loaded PMMA not only did not deteriorate the widely accepted clinical usability of the cement, but also imparted antibacterial and bioactive properties to the cement, with only a low dosage of GS administered locally. This also renders the bioactive antibacterial PMMA cement developed in this study a promising strategy for treating challenging orthopedic infections such as PJI and spinal tuberculosis [32,33].

Generally speaking, bacterial infection or chronic inflammation can alter the normal microenvironment surrounding a focus, turning it into an acidic condition. A local pH value below 6.5 can enhance the activity of osteoclasts, further disrupting bone homeostasis [34–36]. Therefore, transforming the infected area from an acidic environment to a weakly alkaline one is crucial for restoring bone homeostasis. By incorporating BSG into the PMMA substrate, ions can still be released, creating an alkaline microenvironment even after immersion in PBS, as depicted in Fig. 2i–l. For the PMMA and B/PMMA groups, the pH value (7.2–7.4) of PBS remained relatively stable throughout the experimental period. However, the pH values for the B/PMMA and B/G/PMMA groups were consistently higher than those of groups without BSG incorporation, with the pH value of PBS in the B/PMMA and B/G/PMMA groups reaching maximal values of 7.79 and 8.56, respectively, after 2 days (Fig. 2i). Subsequently, the accumulated release of ions (BO_3^{3-}, SiO_3^{2-}, Ca^{2+}, and Sr^{2+}) and GS from the groups was measured. The ion release profiles of groups with BSG incorporation all showed a tendency of a dramatic increase during the initial immersion period, followed by a relative plateau at later immersion times (Fig. 2j and k; Figs. S3b and c). The results of the accumulated release of GS from the G/PMMA and B/G/PMMA groups indicated that the B/G/PMMA group exhibited both a faster release rate and a maximum GS concentration (422.99 μg/mL) after an immersion time of 3 days (Fig. 2l). Notably, the B/G/PMMA group consistently displayed a higher pH value of PBS, a higher accumulated concentration of ions, and a more efficient GS release from the PMMA matrix throughout the entire observation period, suggesting a

synergistic effect between BSG and GS in bioactive antibacterial PMMA cement.

3.2. *In vitro evaluation of antibacterial capacity of bioactive antibacterial PMMA cement*

To further investigate the broad antimicrobial effectiveness of bioactive antibacterial PMMA cement, bacterial suspension of *S. aureus*, *methicillin-resistant Staphylococcus aureus* (*MRSA*), and *Escherichia coli (E. coli)* (5×10^7 CFU/mL) was seeded onto the surface of the cements (3 mm in thickness and 10 mm in diameter) and cultured for 6 h. The results demonstrated fewer bacterial colonies for the B/PMMA and B/G/PMMA groups (*S. aureus*, *MRSA*, and *E.coli*) compared to the PMMA and G/PMMA groups (Fig. 3a and b; Figs. S4a–c). The Alamar Blue reagent was used to further detect bacterial viability. The results indicated that the PMMA group had no inhibitory effect on the bacteria, whereas the G/PMMA group exhibited satisfactory inhibition against *S. aureus*, *E.coli*, and *MRSA* (approximately 50 % inhibition). Furthermore, with the incorporation of BSG, the cement showed more significant damage to *S. aureus*, *MRSA*, and *E.coli,* and the B/G/PMMA cement demonstrated the most effective inhibition in these bacterial strains (Fig. 3c; Fig. S4d). These data imply that the bioactive antibacterial PMMA cement is a broad-spectrum fungicide.

To further explore the effects of bioactive antibacterial bone cement on bacterial biofilm and its morphological structure, as well as the mechanisms behind these effects, we would focus on *S. aureus* as the key research object. Pathogens can evade the action of antibiotics and escape the immune response through biofilm formation, leading to local persistent recurrent infections [37,38]. Biofilm eradication of cements was evaluated by Live (green)/Dead (red) staining, and the disruption of bacterial morphology was evaluated using SEM. After 12 h of incubation, as shown in Fig. 3d, the 2D and 3D images of the PMMA group depicted large areas of green fluorescence, indicating little or even no killing of *S. aureus*. With GS loading, the G/PMMA group showed fewer areas of green fluorescence. In the B/PMMA group, significantly fewer areas of green fluorescence were observed, demonstrating better bacteria-killing effects for cement with BSG incorporation. Particularly, the synergistic interaction between BSG and GS loading resulted in the strongest antibacterial ability in the B/G/PMMA group, with a prominent red fluorescence signal, indicating dead bacteria. Similar observations were also made from the morphology of bacteria. As shown in Fig. 3e, the damage to the cell wall and membrane of *S. aureus* cultured with B/PMMA and B/G/PMMA groups was more severe, leading to irregular and distorted morphology. *S. aureus* co-cultured with PMMA and G/PMMA groups still exhibited healthy, spherical, and intact morphology, as indicated by the red arrows in Fig. 3e. Comprehensively, these data suggest that both B/PMMA and B/G/PMMA cements effectively inhibit *S. aureus*, damage cell walls and membranes, and impair biofilm formation. Most importantly, B/G/PMMA cement consistently showed the best efficiencies in these assays.

3.3. *Transcriptomic analysis of S. aureus after cultured with cements*

As enlightening by the synergistic antibacterial activity of BSG incorporation and GS loading in PMMA cement, RNA transcriptome sequencing (RNA-Seq) was performed to analyze the interaction between bioactive antibacterial PMMA cements and *S. aureus*. For GS, its mechanism against *S. aureus* is as clear as crystal (binding with the 30S subunit of ribosomes to interfere with translation) [39]. Therefore, only PMMA, B/PMMA, and B/G/PMMA cements were selected to culture with *S. aureus* for further RNA-Seq analysis. Comparing the results, there

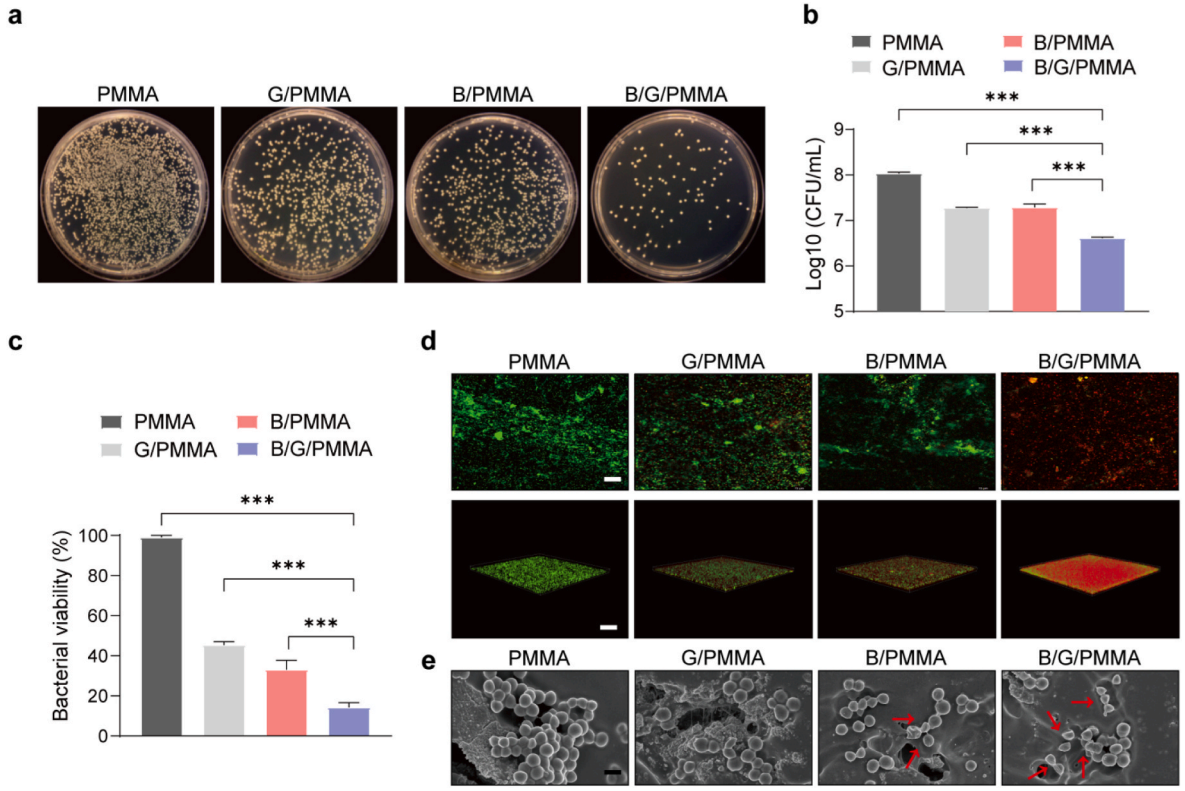

Fig. 3. *In vitro* evaluation of the antibacterial capacity of bioactive antibacterial PMMA cement against *S. aureus*. (a) Optical images of colony formation by *S. aureus* and (b) the quantitative analysis of colony formation. (c) Activity testing of *S. aureus* after 6 h of culture on the surface of cement samples using the Alamar Blue reagent (excitation wavelength: 560 nm; emission wavelength: 590 nm). (d) Live/Dead staining (scale bar = 75 μm) and (e) morphology (scale bar = 2 μm) of *S. aureus* following 6 h of culture on the surface of cement samples. Data are presented as means ± SD. Error bars indicate the standard deviation (n = 3). *P* values were calculated by one-way ANOVA with Tukey's post hoc test and Student's t-test; $^{ns}P > 0.05$, $^{*}P < 0.05$, $^{**}P < 0.01$, $^{***}P < 0.001$.

were 164 differentially expressed genes (DEGs) that were up-regulated and 115 DEGs that were down-regulated between the PMMA group and the B/PMMA group (Fig. 4a; Fig. S5a). The principal component analysis (PCA) revealed a relatively low similarity between these two groups (Fig. S5b). Similarly, for the B/PMMA and B/G/PMMA groups, 843 DEGs were up-regulated, and 744 DEGs were down-regulated. In total, there were 890 up-regulated DEGs and 766 down-regulated DEGs between the PMMA group and the B/G/PMMA group. Furthermore, the DEGs in the three groups were illustrated on a Venn diagram, indicating a clear collaborative effectiveness (Fig. 4c). To initially assess the biological process differences, Gene Ontology (GO) analysis was first conducted. Results showed that, the up-regulated genes of *S. aureus* in the PMMA group and the B/PMMA group respectively, were mainly enriched in ion transport (GO:0006811), lipoteichoic acid biosynthetic process (GO:0070395), and translation (GO:0006412); while the down-regulated ones were mainly enriched in the cell adhesion (GO:0007155), carotenoid biosynthetic process (GO:0016117), response to toxic substance (GO:0009636), and cell wall (GO:0005618) (Fig. S6a,b and Fig. S8a,b). The Gene Set Enrichment Analysis (GSEA) also revealed that, compared with the PMMA group, the transmembrane transport, ion transport, integration component of membrane, and transmembrane transporter activity of *S. aureus* were significantly increased in the B/PMMA group (Fig. 4d).

Compared to the G/PMMA group, the up-regulated genes of *S. aureus* in the B/G/PMMA group were primarily enriched in transmembrane transport (GO:0055085), translation (GO:0006412), ribosome (GO:0005840), and extracellular region (GO:0005576), while the down-regulated ones were enriched in tricarboxylic acid cycle (TCA cycle) (GO:0016021), carotenoid biosynthetic process (GO:0016117), proton-transporting ATP synthase complex, catalytic core F(1) (GO:0045261), Nicotinamide adenine dinucleotide phosphate (NADP) binding (GO:0050661), and Nicotinamide adenine dinucleotide (NAD) binding (GO:0051287) (Figs. S7a and b). These data indicate that when *S. aureus* first encounters BSG in B/G/PMMA cement, it immediately experiences substantial damage to its cell wall and membrane structure due to an ions and alkaline microenvironments. As the bacterial structure is further damaged by BSG degradation, the diffusion of GS into bacterial cells is enhanced, resulting in an increased antibacterial effect through GS's self-mechanism.

To further elaborate on the effects of degradation products of BSG against *S. aureus*, a Kyoto Encyclopedia of Genes and Genomes (KEGG) analysis was conducted (Fig. 4e and f). After comparing the results between PMMA and B/PMMA cements, it was revealed that the up-regulated genes of *S. aureus* were mainly enriched in the ribosome (ko03010), ATP-binding cassette (ABC) transporters (ko02010), phosphotransferase system (PTS) (ko02060), and two-component system (ko02020); the down-regulated ones were mainly enriched in quorum sensing (ko02024), peroxisome (ko04146), and carotenoid biosynthesis (ko00906). This indicates that the microenvironments of BSG degradation can disrupt membrane transporters and weaken antioxidant parts of *S. aureus*, subsequently activating the self-adaptation mechanism of *S. aureus* to cope with adverse extracellular environments.

After comparing the relevant results between B/PMMA and B/G/PMMA cements, it was also found that the up-regulated genes of *S. aureus* were mainly enriched in ribosome (ko03010), ABC transporters (ko02010), and drug metabolism (ko00983); the down-regulated ones were mainly enriched in biofilm formation (ko05111), carotenoid biosynthesis (ko00906), TCA cycle (ko00020), and pyruvate metabolism (ko00620) (Fig. 4g and h). This suggests that the complex microenvironment constructed from BSG degradation and GS release can damage membrane structure, weaken antioxidant components, and inhibit ATP synthesis of *S. aureus*. Moreover, the protein-protein interaction (PPI) network map demonstrated that the DEGs of various biological processes against *S. aureus* were interconnected into a dense functional network (Fig. 4i–k), indicating synergistic antibacterial activities of PMMA cement with higher efficiency due to simultaneous BSG and GS loading.

Overall, when exposed to external damaging environments, *S. aureus* simultaneously initiates both damage pathways and anti-damage pathways, thereby enhancing its self-resistance to harmful stimuli [40]. Interestingly, the bioactive antibacterial PMMA cement exhibits a particularly heightened environmental responsiveness in *S. aureus*.

3.4. Antibacterial mechanism of bioactive antibacterial PMMA cement

3.4.1. Promoting of membrane permeability and biofilm eradication

To explore the mechanism by which BSG damages *S. aureus*, a heat map was generated based on significantly enriched DEGs (Fig. 5a). Previous studies have reported that biomaterials can disrupt the integrity of bacteria through pathways involving cell membrane damage [41]. Lipopolysaccharide (LPS), which carries a negative charge, is present on bacterial cell walls. Positively charged cations from bioactive materials can induce damage to bacterial cell walls and membranes through LPS-activated biological processes [41,42]. Additionally, bacteria maintain a transmembrane proton electrochemical gradient, where extracellular hydrogen ions (H^+) are more abundant than intracellular ones. By being transported into the cell and binding to F-type H^+-ATPase on the cell membrane, H^+ outside the cell activates ATP synthesis. However, in an alkaline environment, extracellular H^+ are neutralized by a large amount of OH^-, thereby inhibiting the ATP synthesis process [43]. As mentioned in Fig. 2j, k and Figs. S3b and c, the degradation of BSG in bioactive antibacterial PMMA cement releases BO_3^{3-}, SiO_3^{2-}, Sr^{2+}, and Ca^{2+}, creating a weakly alkaline microenvironment around implants, which is crucial for inhibiting bacterial activity. Importantly, the release of GS could further enhance BSG degradation in PMMA, leading to an even greater improvement in its antibacterial properties.

Biofilms possess the capability to impede antibiotic penetration, thereby shielding internal colonies and continuously releasing pathogens into the surroundings. This serves as the underlying cause for the persistent infections observed around implants [44]. In the B/PMMA group, the expression of the *MJ1504* gene of *S. aureus*, associated with bacterial biofilms, was up-regulated due to sudden changes in the external environment. Upon the introduction of low doses of GS into BSG/PMMA cement, genes such as *MJ1504*, *MMP0706*, *BSU35660*, and *SaurJH1_2208*, which are related to bacterial cell wall and membrane, showed decreased expression levels (Fig. 5a). To further investigate bacterial cell and membrane damage, protein concentration measurements and o-Nitrophenyl β-D-galactopyranoside (ONPG) testing were conducted. As depicted in Fig. 5b and c, increased protein leakage and ONPG entry into *S. aureus* in both the B/PMMA group and the B/G/PMMA group provided a clearer understanding of cell wall and membrane destruction, particularly in the latter case, indicating a synergistic effect between 30 wt% BSG and 1 wt% GS. Additionally, the cement's ability to eliminate biofilms was evaluated through crystal violet staining. The results showed that after 6 h of cultivation, the *S. aureus* in the B/G/PMMA group exhibited the least purple-stained areas, followed by the G/PMMA group and the B/PMMA group, while the PMMA group displayed the most purple-stained areas (Fig. 5d and e).

The above data indicate that bioactive antibacterial PMMA cement can enhance biofilm eradication by incorporating low doses of GS, compared to B/PMMA cement. What is even more noteworthy is that, unlike drug release in the short term, the BSG in PMMA not only releases substances in the early stages of implantation but also exhibits long-term release properties. This is a crucial aspect for monitoring infections over time.

3.4.2. Interference with membrane transport protein complex

The phosphotransferase system (PTS) is a protein functional complex widely present on the cell membranes of bacteria, catalyzing the intracellular transport of nutrients via a phosphate cascade reaction [45]. ABC transporters are also involved in the absorption and metabolism of

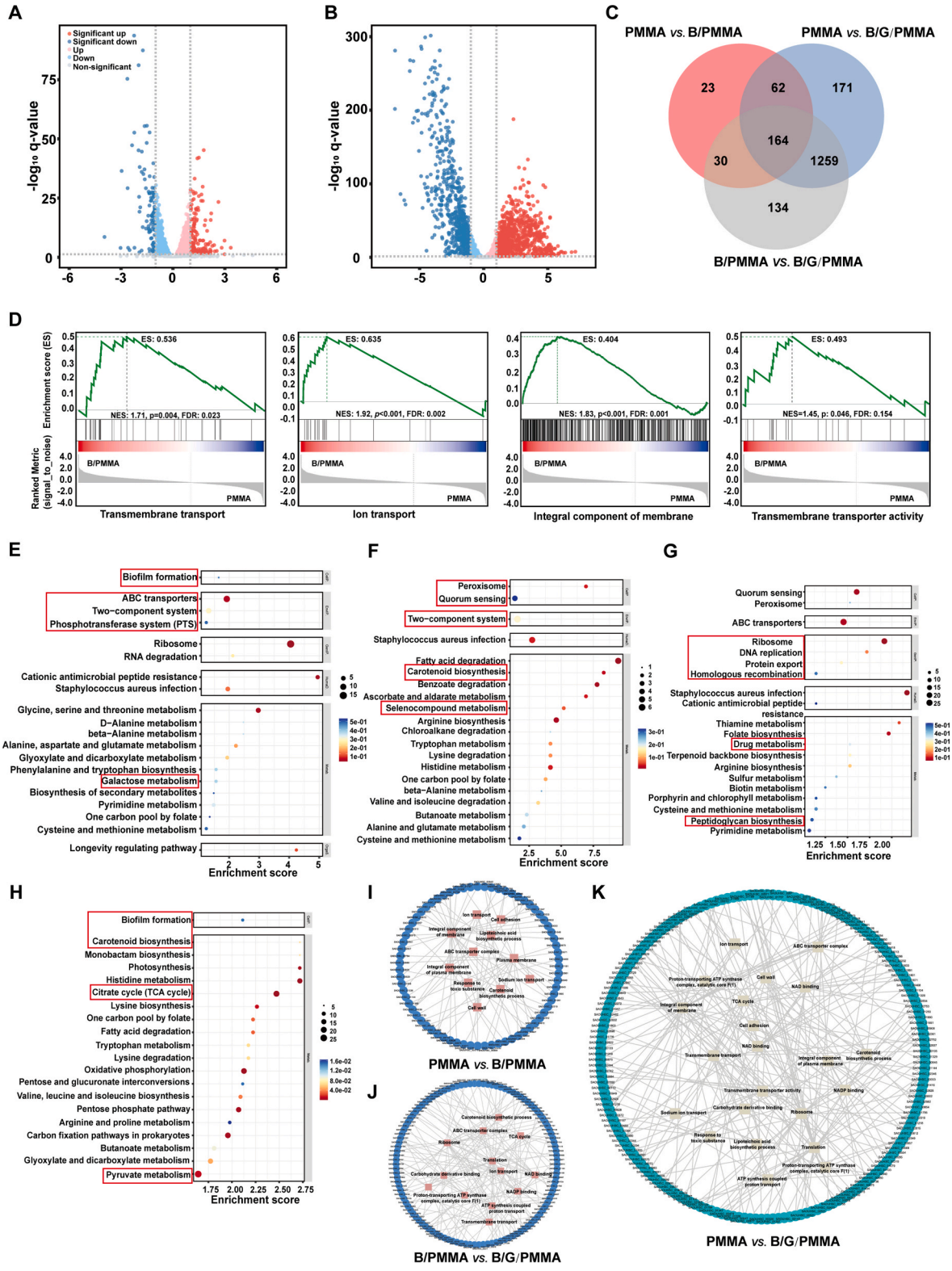

Fig. 4. Transcriptomic analysis of *S. aureus* after being cultured with cements. The volcano plot shows gene expression differences between PMMA and B/PMMA groups (a), as well as between B/PMMA and B/G/PMMA groups (b). (c) Venn diagram of differentially expressed genes. (d) Transmembrane transport, ion transport, integral component of membrane, and transmembrane transporter activity in *S. aureus* between PMMA and B/PMMA groups analyzed by Gene Set Enrichment Analysis (GSEA). (e) Up-regulated genes and (f) down-regulated genes of *S. aureus* compared between PMMA and B/PMMA groups using Kyoto Encyclopedia of Genes and Genomes (KEGG) analysis. (g) Up-regulated genes and (h) down-regulated genes of *S. aureus* compared between B/PMMA and B/G/PMMA groups using KEGG analysis. (i–k) Connections between biological processes shown by the protein-protein interaction (PPI) network map.

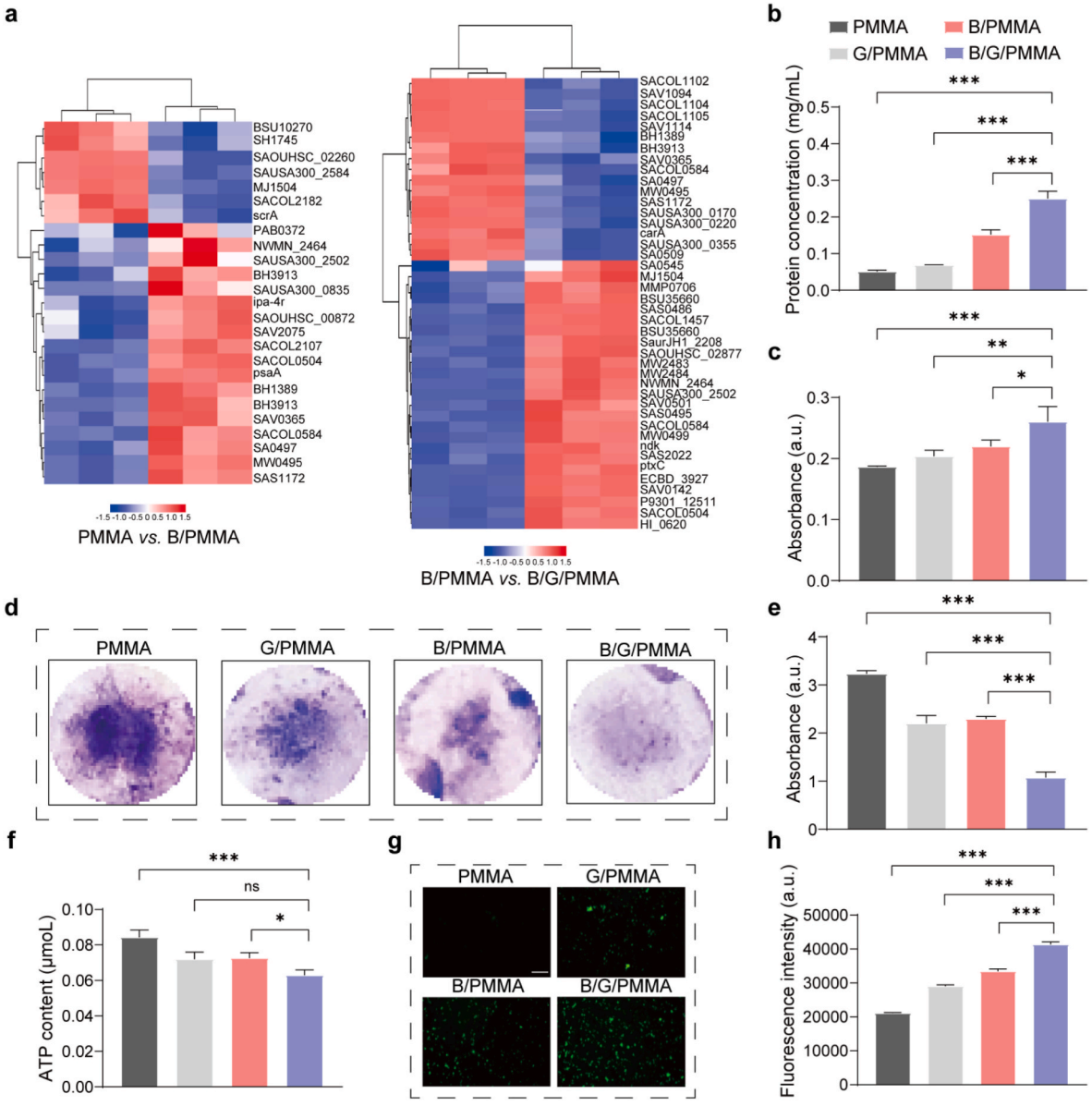

Fig. 5. Antibacterial mechanism of bioactive antibacterial PMMA cement. (a) Pathway changes among groups. Bacterial membrane permeability examined by protein concentration testing (b) and o-Nitrophenyl β-D-galactopyranoside (ONPG) assay (c). (d) Crystal violet staining of biofilm and (e) its quantitative analysis at 562 nm. (f) ATP quantitative analysis at 595 nm. (g) The reactive oxygen species (ROS) levels examined by 2,7-dichlorofluorescein diacetate (DCFH-DA) and (h) its quantitative analysis, with excitation wavelength: 480 nm and emission wavelength: 525 nm, scale bar = 50 μm. Data are presented as means ± SD. Error bars represent the standard deviation. *P* values were calculated by one-way ANOVA with Tukey's post hoc test and Student's t-test. n = 3, $^{ns}P > 0.05$, $^{*}P < 0.05$, $^{**}P < 0.01$, $^{***}P < 0.001$.

extracellular nutrients [46]. This study found that, compared with the PMMA group, the expression of PTS genes (*SACOL2182* and *scrA*) and ABC transporter genes (*psaA*, *lmo1848*, and *BH1389*) in *S. aureus* were significantly increased in the B/PMMA group. By incorporating low doses of GS into B/PMMA cement, the levels of ABC transporter-related genes (*ptxC*, *ECBD_3927*, *SAV0142*, *P9301_12511*, *SACOL0504*, and others) in *S. aureus* in the B/G/PMMA group were further enhanced (Fig. 5a). This indicates that BSG degradation could inhibit *S. aureus* uptake and absorption of nutrients by damaging the cell wall and membrane, thereby increasing the expression of membrane transporter genes in *S. aureus* through a feedback effect. These processes could be potentiated by GS doping.

3.4.3. Prevention of energy metabolism

Energy metabolism plays an important role in the maintenance of life processes and molecular functions. Bacterial ATP synthesis mainly occurs through the electron transport respiratory chain on cell membranes [47,48]. In our results, *SACOL1102*, *SAV1094*, *SAV1114*, *BSU28450*, etc., relative to genes involved in the TCA cycle, were significantly downregulated in *S. aureus* in the B/G/PMMA group. The expression of NADP binding-related genes (such as *USA300HOU_0929*, *BSU32260*, and *SAHV_2356*) was synchronously downregulated in the B/PMMA group. Additionally, NAD binding-related genes, for example, *MMP0706*, *SA1517*, *MW1630*, in *S. aureus* were also inhibited in the B/G/PMMA group, indicating a synergistic inhibition of ATP synthesis between 30 wt% BSG and 1 wt% GS. In the ATP testing, it was shown that the B/G/PMMA group exhibited the most significant inhibitory effect on ATP synthesis compared to other groups (Fig. 5f), further confirming that bioactive antibacterial PMMA cement can achieve ideal antibacterial results by interfering with energy metabolism.

3.4.4. Enhancing oxidative stress

Reactive oxygen species (ROS), as oxidative stress substances, are natural by-products of normal intracellular metabolism [49]. Peroxidase is a common oxidoreductase enzyme, primarily responsible for converting hydrogen peroxide (H_2O_2) and oxygen into water and oxygen [50]. Carotenoids, on the other hand, are part of a non-enzymatic antioxidant pathway. Their antioxidant mechanism primarily involves eliminating ROS to impede and halt the reaction chain by quenching singlet oxygen and dissipating energy in the form of heat [51].

In our results, the expression of peroxisome-related genes (*BSU10270* and *PAB0372*) and carotenoid-related genes (*NWMN_2464* and *SAUSA300_2502*) in the B/PMMA group of *S. aureus* was downregulated, suggesting that BSG degradation can inhibit the antioxidant pathways of *S. aureus*. This, in turn, may have been a contributor to increased intracellular ROS production. As shown in Fig. 5g, the green fluorescence (DCF) intensity gradually increased from the PMMA group to the B/PMMA group, and further to the B/G/PMMA group. A quantitative analysis further revealed that *S. aureus* in the B/G/PMMA group had the highest ROS levels compared to other groups (Fig. 5h), indicating significant oxidative stress damage due to the combined effect of 30 wt% BSG and 1 wt% GS in PMMA against *S. aureus*.

3.4.5. Activation of environmental adaptive mechanisms

The two-component system is an environmental self-adaptive

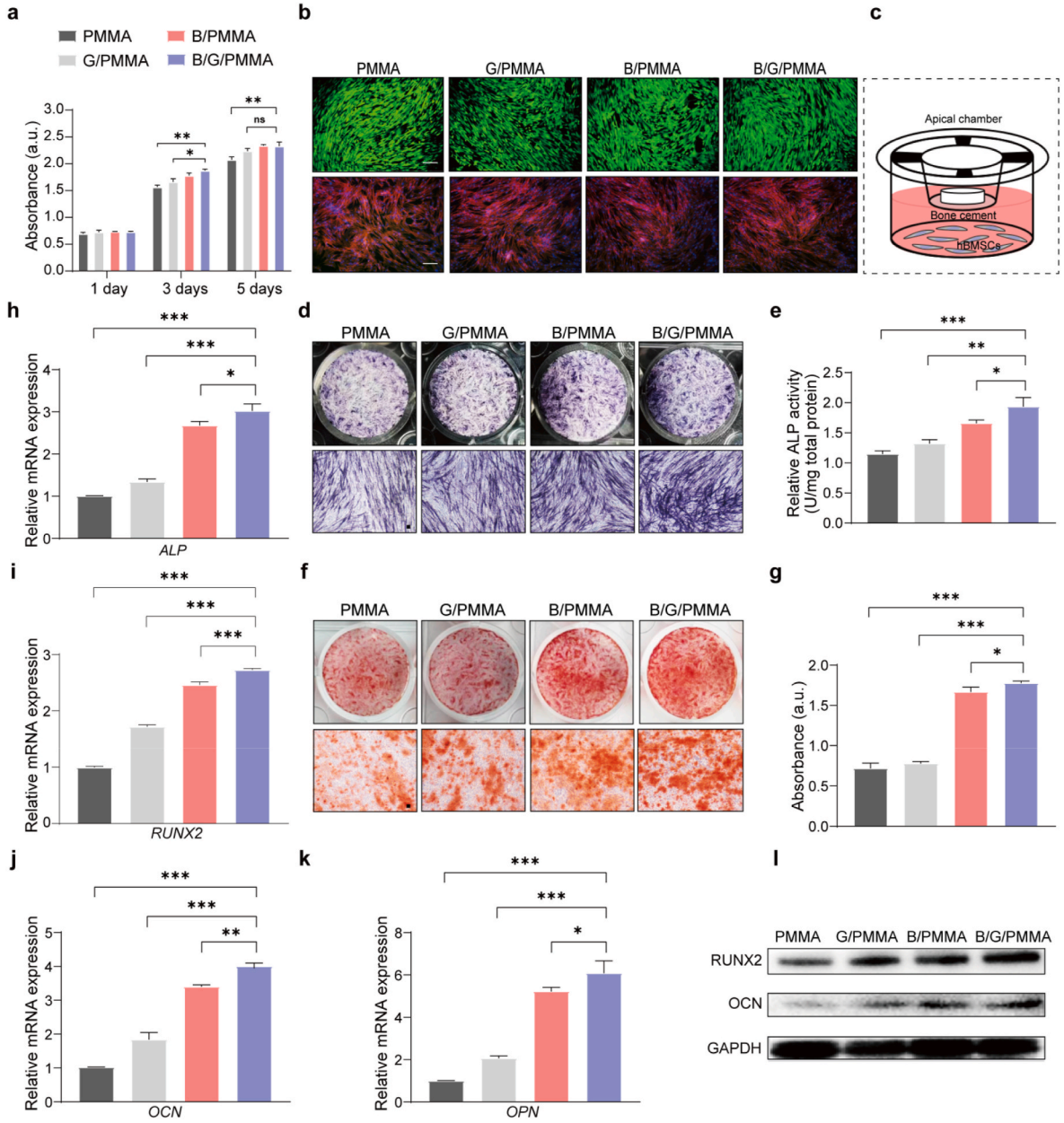

Fig. 6. *In vitro* evaluation of osteogenic differentiation of hBMSCs after being cultured with cements. (a) Cytotoxicity and proliferation of hBMSCs after 1 day, 3 days, and 5 days of co-culture time. (b) Live/Dead (scale bar = 200 μm) and cytoskeleton staining (scale bar = 50 μm) of hBMSCs after a co-culture time of 24 h. (c) Schematic diagram illustrating the co-culture mode. (d) Alkaline phosphatase (ALP) staining of hBMSCs, scale bar = 50 μm. (e) Quantitative analysis of ALP in cell medium after a culture time of 7 days. (f) Alizarin Red S (ARS) staining of hBMSCs after a co-culture time of 14 days, scale bar = 50 μm. (g) Quantitative analysis of ARS staining of hBMSCs. (h) *Alkaline phosphatase* (*ALP*) and (i) *runt-related transcription factor 2* (*RUNX2*) gene expression of hBMSCs after a co-culture time of 7 days. (j) *Osteocalcin* (*OCN*) and (k) *osteopontin* (*OPN*) gene expression of hBMSCs after a co-culture time of 14 days. (l) RUNX2 and OCN protein secretions of hBMSCs after co-culture times of 7 days and 14 days, respectively. Data were presented as means ± SD. Error bars represent the standard deviation. *P* values were calculated by one-way ANOVA with Tukey's post hoc test and Student's t-test. n = 3, $^{ns}P > 0.05$, $^{*}P < 0.05$, $^{**}P < 0.01$, $^{***}P < 0.001$.

mechanism in bacteria. Consisting of histidine kinases and response regulators, it endows bacteria with the ability to perceive and respond to the environment [52]. As shown in Fig. 5a, two-component system--related genes (*MJ1504*, *BH3913*, *SAV2075*, and *SACOL2107*) in *S. aureus* were significantly upregulated in the B/PMMA group, indicating that BSG degradation activates an emergency repair mechanism in *S. aureus*. Fig. 5a also indicates that ribosome-related genes, such as *SAV0365*, *SACOL0584*, *SA0497*, and *MW0495*, in the B/PMMA group were significantly upregulated in *S. aureus*. This implies an increased protein expression in response to a destructive stimulus in *S. aureus*. After adding 1 wt% GS to 30 wt% BSG/PMMA, genes like *SAV0501*, *SACOL0584*, *SA0497*, and *MW0495* were further strengthened, indicating that the remedial repair pathway in *S. aureus* was activated by feedback, and GS took effect through its antibacterial mechanism—binding to the ribosome 30S subunit and inhibiting its function.

3.5. In vitro evaluation of osteogenic differentiation of hBMSCs after cultured with cements

The cytotoxicity and proliferation of hBMSCs after co-culturing with cements were investigated, and the results demonstrate that all cements showed no obvious cytotoxicity on hBMSCs at 24 h after co-culture (Fig. 6a). Moreover, Live/Dead staining and cytoskeleton staining further confirmed the positive cell viability of hBMSCs in all groups after 24 h (Fig. 6b). At 3 and 5 days after co-culture, cement with BSG incorporation (B/PMMA and B/G/PMMA groups) promoted the proliferation of hBMSCs. The B/G/PMMA group exhibited a notably higher optical density (OD) value than that of the B/PMMA group (Fig. 6a), indicating a synergistic effect on hBMSCs proliferation when both BSG and GS were loaded into the PMMA cement. Subsequently, osteogenic differentiation and biomineralization of hBMSCs were further assessed. The schematic diagram of the co-culture mode between cement samples and hBMSCs is presented in Fig. 7c. After incubation for 7 days, hBMSCs in both the B/PMMA and B/G/PMMA groups displayed a larger alkaline phosphatase (ALP) staining area (Fig. 6d) and higher ALP activity in the medium (Fig. 6e). Additionally, hBMSCs in the B/G/PMMA groups showed the optimal osteogenic differentiation function. At 14 days after co-culture, hBMSCs in both the B/PMMA and B/G/PMMA groups displayed better biomineralization performance in Alizarin Red S (ARS) staining, as evidenced by a larger staining area and higher absorbance in Fig. 6f and g, respectively. Furthermore, hBMSCs in the B/G/PMMA groups still had the optimal biomineralization function among the groups.

The initial findings suggested that the release of GS from G/PMMA and B/G/PMMA cements may have facilitated the proliferation, osteogenic differentiation, and biomineralization of hBMSCs. To further investigate and confirm these effects, a series of culture media with varying GS concentrations (1600 μg/mL, 800 μg/mL, 400 μg/mL, 200 μg/mL, 100 μg/mL, 50 μg/mL, and 25 μg/mL) were prepared. The results indicated that GS can indeed enhance the cellular function of hBMSCs, but only within specific concentration ranges. After 24 h of culture with GS, a significant reduction in hBMSC proliferation was observed at concentrations exceeding 400 μg/mL (Fig. S9a). After 7 days, ALP staining revealed a decline in osteogenic differentiation of hBMSCs in media with GS concentrations greater than 100 μg/mL (Fig. S9b). After 14 days, ARS staining showed no significant calcium deposition in hBMSCs cultured in media with GS concentrations above 200 μg/mL (Fig. S9c). Conversely, when GS concentrations were below 50 μg/mL, all hBMSC groups exhibited significant calcium deposition in ARS staining (Fig. S9c). Thus, it can be concluded that GS indeed influences the osteogenic function of hBMSCs in a concentration-dependent manner.

In addition, we assessed the expression of osteogenic-related genes and proteins following co-culture with cements. The results demonstrated a significant up-regulation in the expression of *ALP* (at a culture time of 7 days), *runt-related transcription factor 2* (*RUNX2*, at a culture time of 7 days), *osteocalcin* (*OCN*, at a culture time of 14 days), and *osteopontin* (*OPN*, at a culture time of 14 days) in hBMSCs when co-cultured with the G/PMMA group, B/PMMA group, and B/G/PMMA group, compared to the PMMA group (Fig. 6h–k). Furthermore, osteogenic-related proteins, including RUNX2 and OCN, were also significantly up-regulated in hBMSCs co-cultured with the B/PMMA and B/G/PMMA groups (Fig. 6l; Fig. S10). These findings suggest that incorporating BSG into cements can enhance the osteogenesis of hBMSCs, with a synergistic effect between BSG and GS, resulting in improved osseointegration of bioactive antibacterial PMMA cement.

In vitro studies of bioactive antibacterial PMMA cement indicate that incorporating BSG represents a practical strategy to achieve efficient antibacterial properties and promote osteogenesis, even at low doses of GS loading, in bioinert PMMA cement. This finding holds promise for clinical treatments of bone infection and related delayed osseointegration.

3.6. In vivo evaluation of antibacterial vitality, osteointegration, and biocompatibility of cements

3.6.1. Antibacterial vitality in vivo

Based on the confirmed antibacterial efficacy observed *in vitro*, the bioactive antibacterial PMMA cements were implanted into a Sprague-Dawley (SD) rat femoral bone marrow infection model to assess their antibacterial performance and osteointegration *in vivo* [53]. Surgical procedures are depicted in Figs. S11 and S12. Detailed experimental plans and timeline information are provided in Fig. 7a. One week after the implantation surgery, the implants were carefully removed without damage and rolled on a standard agar plate for five rounds [54]. The implants were then placed in a sample bottle (105 mm × 27.5 mm) containing Luria-Bertani medium. These bottles were incubated at 37 °C for 24 h to evaluate the bacterial loading on the implants. Simultaneously, the degree of infection and bone destruction were assessed by X-ray scanning. Two weeks after the implantation surgery, the antibacterial efficacy of the implants was further evaluated through X-ray scanning, Hematoxylin-eosin (H&E) staining, Gram staining, and Masson staining.

As demonstrated in Fig. 8b and c, the implants from the pure PMMA group harvested from rats presented a large number of bacterial colonies, indicating that pure PMMA cement did not exhibit antibacterial activity *in vivo*. Incorporation of BSG demonstrated superior antibacterial activity compared to GS-loaded PMMA cement, as evidenced by significantly fewer bacterial colonies in the B/PMMA and B/G/PMMA groups. Consistent with the *in vitro* antibacterial results, the B/G/PMMA group showed the fewest bacterial colonies among the groups. The OD value of the medium co-cultured with the retrieved implants confirmed the inhibition of biofilm formation by the cement *in vivo*, and the trend was consistent with the results of the standard agar plate experiments, as depicted in Fig. 8d.

X-ray imaging directly visualized the extent of infection diffusion and bone destruction. The results indicated that the PMMA cement group exhibited the most significant bone infection diffusion and periosteal response, as evidenced by the worst blurred field of vision one week after the operation (Fig. 7e). Conversely, groups implanted with B/PMMA and B/G/PMMA cement showed slight or even no signs of periosteal reaction or diffuse lesions (red arrow). The following radiographic changes were evaluated for each sample: 1) osteolysis, 2) soft tissue swelling, 3) periosteal reaction, 4) general impression, and 5) deformity. Scores were assigned according to the following criteria: 0 = absent, 1 = mild, 2 = moderate, or 3 = severe. These scores were then summed, with the highest possible total score being 15. The final X-ray score was averaged among three evaluators [55]. The score showed the lowest value of 3.6 ± 0.1 for the B/G/PMMA group and the highest value of 7.9 ± 0.3 for the PMMA group (Fig. 7f). The above results indicated that bioactive antibacterial PMMA cement can immediately reduce *S. aureus* viability, thereby avoiding subsequent obvious deeper infection and

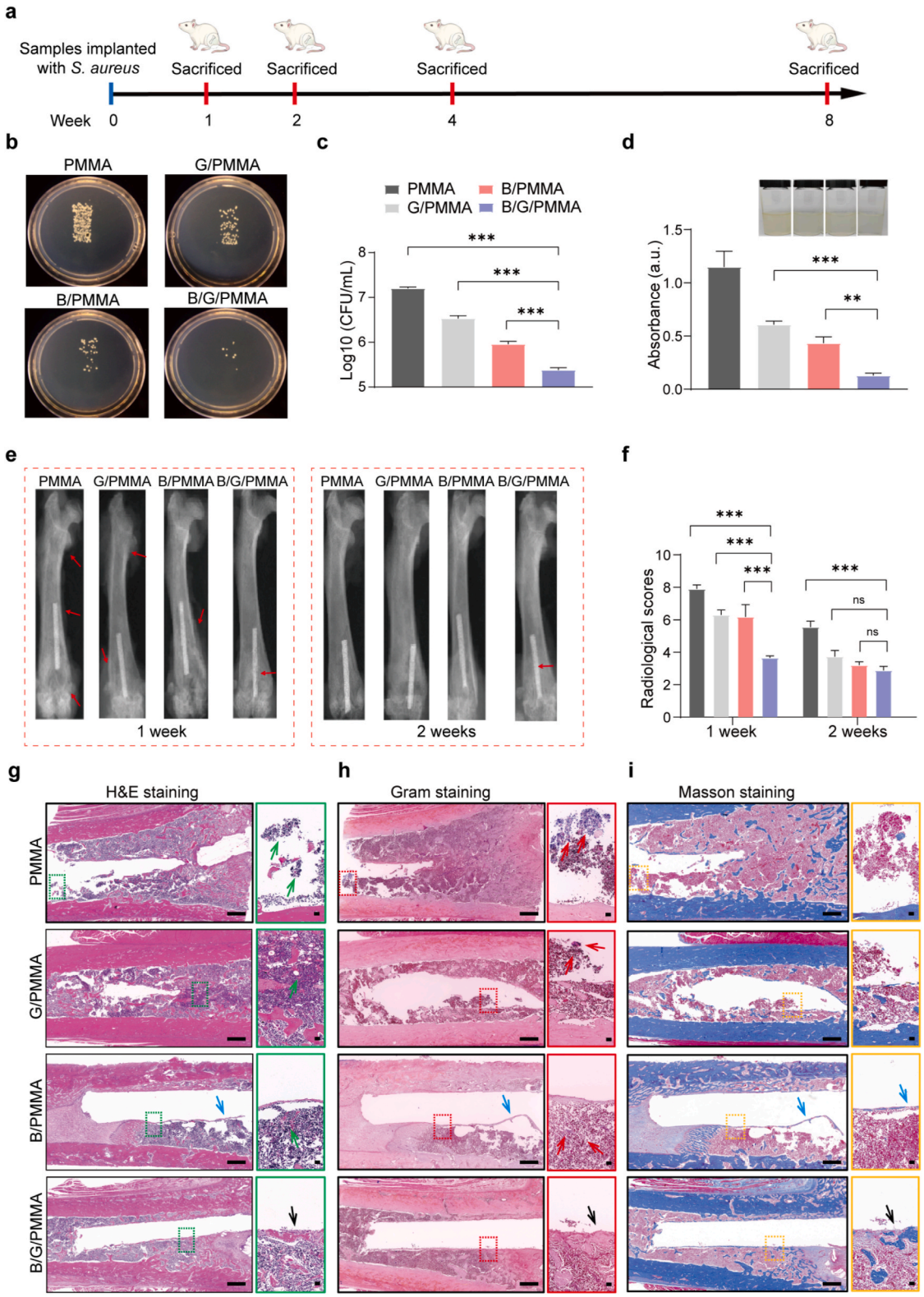

Fig. 7. *In vivo* evaluation of the antibacterial vitality of cements. (a) Schematic diagram of the experimental design *in vivo*. (b) Colonies formation under the agar plate method at 1 week after the implantation surgery. (c) Quantitative analysis of colonies formation using the agar plate method. (d) Evaluation of the antibacterial effect at 1 week after the implantation surgery using the bacterial culture method (OD = 600 nm). (e) Radiographs of focal lesions in *S. aureus*-infected rat femurs after cements were implanted for 1 week and 2 weeks post-implantation surgery. (f) The histogram of radiographic scores. (g) Hematoxylin-eosin (H&E) staining, (h) Gram staining, and (i) Masson staining at 2 weeks after the implantation surgery. Scale bar for overview = 500 μm, scale bar for bone-cement interface = 200 μm. Data were presented as means ± SD. Error bars represent the standard deviation. *P* values were calculated by one-way ANOVA with Tukey's post hoc test and Student's t-test. n = 4, $^{ns}P > 0.05$, $^{*}P < 0.05$, $^{**}P < 0.01$, $^{***}P < 0.001$.

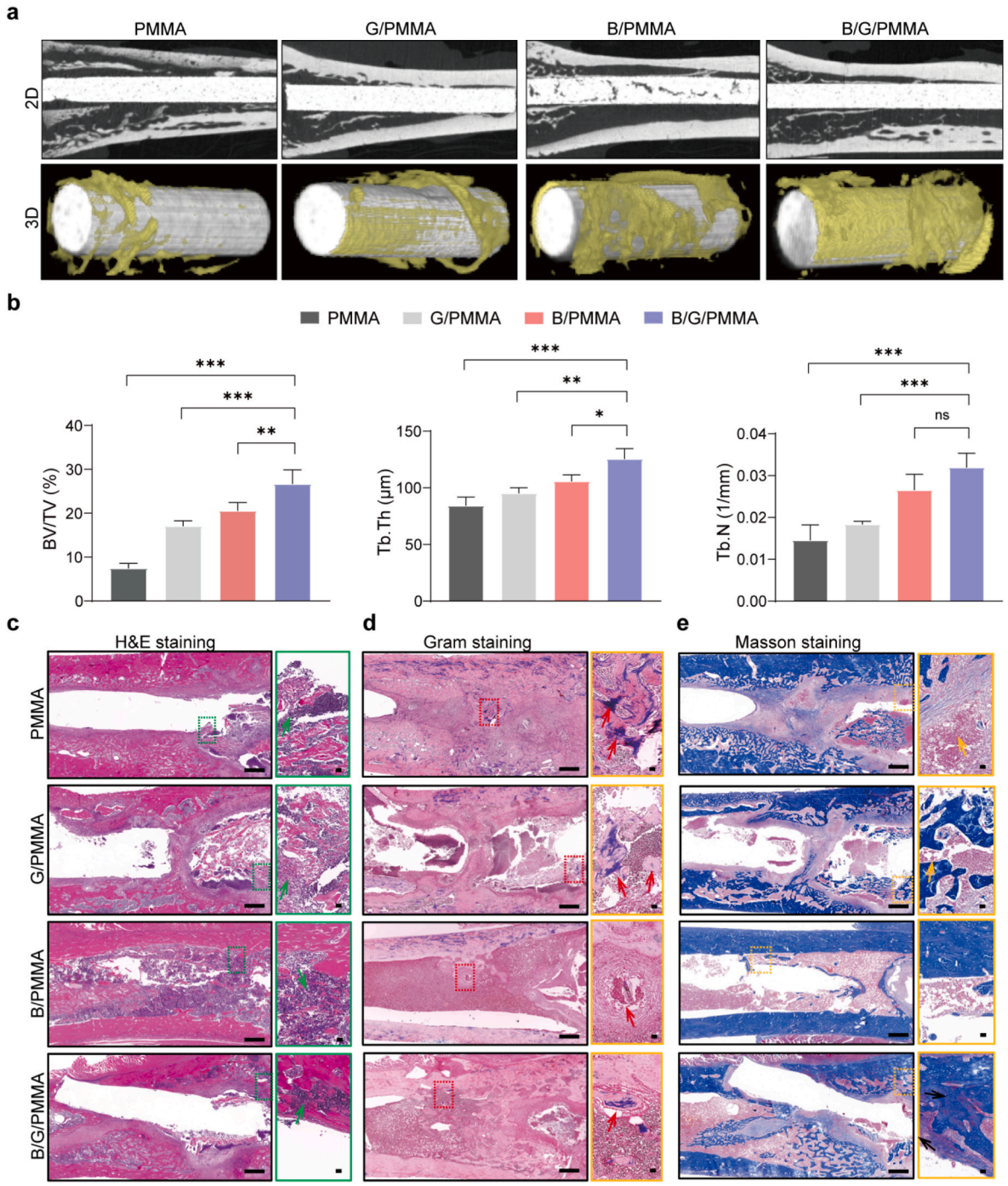

Fig. 8. *In vivo* evaluation of the antibacterial ability and osteointegration of cements. (a) Sagittal and 3D reconstructed images of rat femurs after cement implantation for 8 weeks. (b) An analysis of bone parameters was conducted eight weeks post-implantation surgery, encompassing measurements of bone volume/total volume (BV/TV), trabecular thickness (Tb. Th), and the number of trabeculae (Tb. N). (c) H&E staining, (d) Gram staining, and (e) Masson staining were performed at 4 weeks after the implantation surgery. Scale bar for overview = 500 μm; scale bar for bone-cement interface = 200 μm. Data were presented as means ± SD. Error bars represent the standard deviation. *P* values were calculated by one-way ANOVA with Tukey's post hoc test and Student's t-test, n = 4. $^{ns}P > 0.05$, $^{*}P < 0.05$, $^{**}P < 0.01$, $^{***}P < 0.001$.

inflammation.

At 2 weeks after the implantation surgery, X-rays revealed that serious bone necrosis had occurred in the PMMA group, as evidenced by low-density shadow areas throughout the entire femur (Fig. 7e). This indicated the persistence and deterioration of bone infection. In contrast, for the groups implanted with G/PMMA cement and B/PMMA cement, the low-density shadow areas were significantly reduced. Notably, the B/G/PMMA group showed no obvious signs of bone necrosis. The radiographic scores were 5.6 ± 0.4 for the PMMA group, 3.8 ± 0.4 for the G/PMMA group, 3.2 ± 0.3 for the B/PMMA group, and 2.8 ± 0.3 for the B/G/PMMA group, respectively. The scores for the B/G/PMMA group were significantly lower than those of the other groups ($P < 0.05$) (Fig. 7f), confirming the superior inhibition of *S. aureus* by bioactive antibacterial PMMA cement *in vivo*.

Except for the B/G/PMMA group, H&E staining revealed a large number of inflammatory cell infiltrates in the femoral medullary cavities

of the PMMA, G/PMMA, and B/PMMA groups (green arrows). Gram staining confirmed that *S. aureus* colonized within the osteocyte lacunar-canalicular network (OLCN) and necrotic bone in the medullary cavities (red arrows). Although the amount of bacterial colonization in the G/PMMA group was less than in the PMMA group, some Gram-positive bacteria were still observed (red arrows), indicating the limited bactericidal efficacy of G/PMMA. In the B/PMMA group, cystic fibrous wrapping around the bioactive bone cement implant was noted (blue arrows), accompanied by a small amount of inflammatory cell infiltration (green arrows) and *S. aureus* colonization within the medullary cavity (red arrows). These findings inevitably lead to sustained infection and high recurrence, imposing great mental and financial burdens on patients [56]. Interestingly, in the B/G/PMMA group, neither inflammatory cell infiltrates nor Gram-positive *S. aureus* were observed in the femoral medullary cavity. Additionally, a large amount of collagen formation was observed around the implant, as evidenced by Masson staining (black arrows), indicating that *S. aureus* bone infection was well controlled in this group (Fig. 7g–i). These results, obtained 2 weeks after the implantation surgery, demonstrate the high efficacy of bioactive antibacterial PMMA cement in healing bacterial infections. *in vivo*.

3.6.2. Osseointegration

To further evaluate the osseointegration of the cements, various methods were employed, including Micro-computed tomography (Micro-CT), H&E staining, Masson staining, and Safranin O-Fast Green staining. The results, depicted in Fig. S13a and Fig. 8a, showcase 3D reconstructed and sagittal section images of the rat femur with implants at 4 weeks and 8 weeks post-implantation surgery. Significantly, it was noted that new bone formation around B/PMMA and B/G/PMMA implants was notably more pronounced, with this newly formed bone developing into a layer of calcium shell structure surrounding the implants. In contrast, for the G/PMMA cements in the rats, only a certain amount of loose and amorphous bone tissue was observed around the implant, with minimal new bone formation detected due to bacterial erosion and osteolysis. Analysis of bone parameters from Micro-CT results, such as bone volume/total volume (BV/TV), trabecular thickness (Tb. Th), and the number of trabeculae (Tb. N), indicated that the BV/TV, Tb. Th, and Tb. N values for the B/G/PMMA group were the highest among all groups (Fig. 8b; Figs. S13b–d). Additionally, BSG and low-dose GS in PMMA consistently exhibited superior bone parameters.

In addition, the infection control and osteointegration of the cements were further evaluated through H&E staining, Gram staining, and Masson staining (Fig. 8c–e; Fig. S14). At 2 weeks after surgery, H&E and Gram staining results revealed a significant amount of inflammatory cell infiltration (green arrows), bacterial colonization within OLCN (red arrows), and destruction of the medullary cavity in both the PMMA and G/PMMA groups. In the G/PMMA group, despite some bacterial presence within the medullary cavity, the bone medullary cavity remained relatively intact and regular, as demonstrated by Gram staining and Masson staining. This group demonstrated effective control of bacterial colonization in the bone canaliculi, with Masson-stained blue collagen formation around the material, indicating that the G/PMMA cement exhibited significant antibacterial efficacy. In the B/G/PMMA group, H&E staining revealed minimal inflammatory cell infiltration and limited Gram-stained bacterial colonization in the medullary cavity. Additionally, there was significant new bone formation around the implant, indicating that bone infection was well-controlled in the B/G/PMMA group. These results suggest that the combined release of low-dose antibiotics and BSG components has excellent potential for controlling *S. aureus* bone infection while promoting osteointegration.

3.6.3. Biocompatibility in vivo

Two weeks after the surgical procedure, the principal visceral organs were excised and subsequently analyzed via H&E staining to evaluate the systemic toxicity of the implants *in vivo*. The results demonstrated no significant damage to the heart, liver, spleen, lungs, or kidneys (Figs. S15 and S16), thereby confirming that the incorporation of BSG and minimal concentrations of GS in PMMA cement did not induce tissue or organ toxicity *in vivo*.

4. Discussion

Currently, when addressing the challenging treatment of *S. aureus* bone infections in clinical practice, despite the development of numerous innovative treatment strategies by orthopedic surgeons and scientific researchers over the past decades, antibiotic-loaded poly (methyl methacrylate) bone cement (ALBC) has been employed as a standardized strategy for the treatment and prevention of various bone infections [57]. However, as the applications of ALBC increase, its drawbacks become increasingly apparent. These include: systemic toxicity, which arises when drug distribution extends beyond the local site and exceeds systemic clearance. Other are local tissue toxicity, the ineffectiveness of commonly used antibiotics against bacteria embedded in biofilms, the emergence of drug resistance resulting from the overuse of local antibiotics, and low antibiotic release rate. Furthermore, due to its lack of biological activity, antibiotic-loaded PMMA bone cement faces challenges in promoting bone ingrowth and osseointegration. Thus, while ensuring the antibacterial efficacy of low-dose antibiotic bone cement, it is of great clinical significance to conduct research aimed at endowing traditional antibiotic bone cement with additional biological properties [58–60].

Bioactive glass (BG), a unique inorganic bioactive material designed by Prof. Larry L. Hench, releases the network ions such as BO_3^{3-}, SiO_3^{2-}, Ca^{2+}, and others while simultaneously creating an alkaline microenvironment upon degradation. This microenvironment regulates polarization, relieves gene and cytokine expression in macrophages, stimulates osteogenic differentiation of bone marrow mesenchymal stem cells, and promotes angiogenesis in endothelial cells [61,62]. The invention of BG has sparked a global healthcare revolution [63], with over 1.5 million patients having been treated with bioactive glass products for a variety of clinical conditions involving hard tissue regeneration [64,65]. Pioneering clinical investigations have also demonstrated the bright potential of BG in the treatment of bone infections. The bioactive glass product, trademarked as S53P4, has shown a high cure rate (>80 %) of infectious bone defects in clinical trials, despite some cases experiencing infection recurrence [66–69]. Marques et al. found that BG could initially suppress biofilm formation, but did not consistently eliminate biofilm formation throughout the entire treatment period. This suggests that bioactive glass has limited antibacterial efficacy against biofilm formation [70].

To explore the suitability of BG for multiple tissue regeneration, boron (B) was introduced into the network structure of BG to regulate its reactivity and degradation rate, yielding a new type of bioactive glass, borosilicate bioactive glass (BSG) [25,26]. Our previous research revealed that BSG significantly enhanced osteointegration and osteogenesis of PMMA cement in both human and goat vertebrae. Furthermore, the formation of a mildly alkaline ion milieu caused by BSG degradation promoted osteogenic expression of MC3T3-E1 cells *in vitro* [27]. However, it remained unclear whether BSG inhibits bacterial growth, and the antibacterial mechanism of BG had not yet been fully elucidated.

By introducing 10 wt%BSG and 30 wt%BSG into PMMA cement, it was found preliminarily that BSG significantly enhanced the antibacterial activity of PMMA. Sufficient incorporation of BSG into PMMA, such as the 30 wt%% BSG/PMMA group, even demonstrated antibacterial activity comparable to that of the highest amount of GS-loaded PMMA cement (like the 10 % GS/PMMA group) when both were cultured with *S. aureus* (Fig. S2). Motivated by the above results, 30 wt% of BSG was incorporated into low-dosage GS-loaded (1 wt%) PMMA cement to successfully construct bioactive PMMA cement (named B/G/PMMA), which showed satisfactory synergistic antibacterial activity *in vitro*.

RNA-Seq results showed that BSG caused greater disruptions to the

cell wall and cell membrane of *S. aureus* (Figs. S6a and b), which is consistent with the activity of bioactive materials previously documented [41–43]. After exposure to bacteria, the bioactive antibacterial PMMA cement immediately released part of the loaded GS and created the ionic and alkaline microenvironment that results from the degradation of BSG. The extracellular ions can firstly destroy the integrity of the bacterial cell wall and membrane structure to a certain extent, while the highly alkaline microenvironment can subsequently interfere with the respiratory chain on the cell membrane, which together disrupt bacterial ATP synthesis and effectively reduce the collective injury tolerance of bacteria, decreasing the secretion of adhesive proteins, thereby achieving inhibition of bacterial colony development and biofilm formation (Fig. 4e,f and Figs. S6a and b). Accompanying the disruption of the cell wall and membrane, the partially released GS that accumulates extracellularly is gradually transported into *S. aureus* through membrane transporters. However, due to the relatively low concentration of intracellular antibiotics present, it is not sufficient to completely block bacterial gene expression. So, even though bacterial activity is inhibited, *S. aureus* can still maintain normal structure and metabolic function. It has been reported that *S. aureus* has evolved a response mechanism by initiating a self-healing system (known as the two-component system) to adapt to these harsh external environments [52]. This activation of the self-healing system may also be a critical factor that prevents complete biofilm elimination when using BSG to kill bacteria. The above statement belongs to the preliminary stage of initial contact and extracellular bacterial inhibition of BSG synergistically reinforce low-dose antibiotic loaded implants combating bacteria (Fig. 9a).

With the continuous degradation of BSG and GS release, the extracellular ionic and alkaline microenvironment was further reinforced, thereby inducing more severe damage to the cell wall and membrane of *S. aureus* (Figs. S7a and b), which further facilitated the release of more ions to be transferred intracellularly. At the same time, the function of nutrient transporters on the membrane, for example, ABC transporters, was inhibited (Fig. 4g and h), which greatly weakened the intracellular transport of substances essential for metabolism, thereby exerting a stronger inhibitory effect on bacterial matter and energy metabolism, further interfering with ATP synthesis [45,46]. More importantly, the ionic and alkaline microenvironment also seriously downregulated the expression of bacterial antioxidant component genes, including those involved in peroxisome and carotenoid biosynthesis, which inevitably induced an imbalance in the oxidative stress response and overproduction of ROS in *S. aureus* [49–51], further causing irreparable damage to the structure of *S. aureus*. This second stage belongs to the process of intracellular accumulation of ions and antibiotics, with bacterial inhibition progressing from extracellular to intracellular, induced by BSG synergistically reinforcing low-dose antibiotic-loaded implants in combating bacteria (Fig. 9b).

As is well known, more severe damage to the cell wall and membrane of bacteria can greatly increase the permeability of the cell membrane to antibiotics, thereby accelerating the transport of antibiotics from extracellular to intracellular. Thus, sufficient GS can be continuously and efficiently accumulated within *S. aureus*. Although *S. aureus* attempts to combat the harsh environment and develop damage tolerance by simultaneous activation of the two-component system (Fig. 4e) at that time, the sufficient intracellular GS can positively impede the synthesis of essential proteins in *S. aureus* through irreversible binding to the 30S subunit of ribosomes. By inhibiting the TCA cycle, NAD, NADP binding activity, ATPase activity, and carotenoid biosynthesis, GS itself can also weaken ATP synthesis within *S. aureus* (Fig. 5f and Figs. S8a and b). By severely damaging the antioxidant systems (such as carotenoid biosynthesis) within *S. aureus*, the decreased ATP synthesis can in turn weaken the antioxidant components [50,51], thereby further inducing a significant increase in intracellular ROS and causing more serious destruction of the bacterial structure. This final stage belongs to intracellular antibacterial activity against *S. aureus*, induced by BSG synergistically reinforcing low-dose antibiotics in implants combating bacteria (Fig. 9c). Previous research has revealed that there is always lipid peroxidation of cell membranes due to intracellular ROS emission [71], but a deficiency in antioxidant components (peroxisome and carotenoid) will hinder the efficient removal of ROS by *S. aureus*. This dilemma then creates a positive feedback loop between increased oxidative stress and antioxidant dysfunction, which obviously lays the foundation for damage to *S. aureus*. There is precedence for investigating the reasons why BSG promotes bacterial alterations, as well as the relationship between BSG and low dosages of GS in PMMA matrix-induced bacterial killing and biofilm clearance. These findings offer an overall understanding of the mechanism of BSG against bacteria and provide a promising remedy for antibiotic-resistant bacteria in the prevention and treatment of bone infections.

From the perspective of ideal healing, the complete eradication of bacteria is not the endpoint but rather a milestone of treatment for orthopedic infections, since osteogenesis activates only after bacteria are restrained. Otherwise, persistent bone resorption caused by bacterial-related inflammation will destroy the structural integrity and physiological function of bone tissue. Therefore, it is crucial to adopt a mindset that implants should sequentially achieve bacteria killing and the healing of relevant bone defects. In this study, the alkaline microenvironment and ions released due to the degradation of BSG also favored the cell functions of hBMSCs, and resulted in significant promotion of viability, proliferation, and osteogenic differentiation of hBMSCs *in vitro*. Furthermore, the expressions of early *(RUNX2)*, middle-term

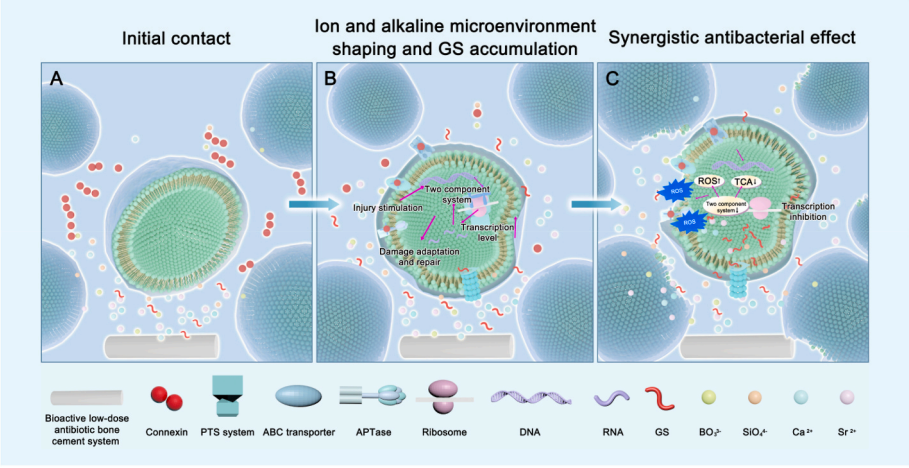

Fig. 9. The mechanism of borosilicate bioactive glass synergistically reinforces low-dose antibiotic-loaded implants in combating bacteria.

(*ALP*), and late-stage (*OCN*) osteogenic genes were significantly upregulated. Moreover, this bioactive antibacterial PMMA cement was shown to enhance osseointegration after completing the antibacterial task without any biosafety concerns *in vivo*, consistent with our previous report [27].

Despite the significant findings presented in this study, several limitations must be acknowledged. Firstly, our study observed the positive effect of low dosages of GS on boosting osteogenic differentiation; however, the underlying mechanism remains unclear. Understanding how low dosages of GS enhance osteogenesis could have significant implications for medication or drug coupling strategies in bone regeneration. Secondly, it is imperative to conduct a thorough biological evaluation in line with ISO 10993 to assess the biosafety of the bioactive antibacterial PMMA cement. Ensuring the biocompatibility and safety of the cement is crucial for its clinical application and patient well-being. Finally, while the use of a small animal model, such as the rat femoral bone marrow infection model employed in this study, provides valuable insights, it may not entirely replicate bone infections in humans. Addressing these limitations through future research endeavors will contribute to the advancement of bioactive antibacterial PMMA cement as a viable treatment option for bone infections and defects, ultimately benefiting patients and healthcare practices.

Even though there are the limitations mentioned above, BSG integration is regarded as a prospective and effective strategy for significantly reducing antibiotic dosage locally or systemically while also offering more potent antibacterial activity and osteogenesis. Furthermore, suitable verification of BSG's antibacterial activity, as well as the preliminary clarification of its antibacterial mechanism, would have far-reaching implications for the usage of BSG in infective tissue treatment. Most importantly, because of its exceptional biological properties and efficient antibiotic capacity, BSG's non-drug antibacterial strategies may be a better substitute in clinical practice than either pure PMMA cement or ALBC. Collectively, the incorporation of BSG into low-dose GS loaded PMMA cement offers a promising and practical strategy for effectively addressing bacterial infections and facilitating bone regeneration.

5. Conclusion

In this study, the incorporation of BSG into low-dose GS loaded PMMA cement offers a promising and practical strategy for effectively addressing bacterial infections and facilitating bone regeneration. The addition of BSG not only maintains the superior mechanical characteristics of PMMA but also introduces beneficial properties, such as an alkaline and ionic microenvironment, resulting from the degradation of BSG. The synergistic effects of BSG and GS within the PMMA cement significantly enhance antibacterial efficacy compared to PMMA cement containing either BSG or GS alone. Mechanistically, the degradation of BSG compromises the integrity of the cell wall and membrane, reduces the activity of antioxidant components (peroxisomes and carotenoids), and impedes ATP synthesis in *S. aureus*. Furthermore, the sustained release of low-dose GS in the vicinity of implants amplifies the antibacterial effects of BSG by inhibiting bacterial translation. Additionally, the combination of BSG and low-dose GS promotes the survival, adhesion, proliferation, and osteogenic differentiation of hBMSCs *in vivo*. Evidence from studies utilizing a rat femoral bone marrow infection model indicates that the incorporation of BSG into low-dose GS loaded PMMA cement results in enhanced synergistic antibacterial activity and improved osseointegration. This study highlights the potential of BSG incorporation in PMMA cement as a practical approach to reduce antibiotic dosage while enhancing antibacterial activity and osteogenesis. These findings hold promise for addressing bacterial antibiotic resistance and treating various infectious bone diseases clinically.

CRediT authorship contribution statement

Mengke Fan: Writing – review & editing, Writing – original draft, Methodology, Investigation, Formal analysis, Conceptualization. **Youliang Ren:** Writing – review & editing, Writing – original draft, Conceptualization. **Yanbin Zhu:** Methodology, Conceptualization. **Hao Zhang:** Conceptualization. **Shuaijie Li:** Methodology, Conceptualization. **Chunyu Liu:** Methodology, Conceptualization. **Hongzhi Lv:** Methodology, Conceptualization. **Lei Chu:** Methodology, Conceptualization. **Zhiyong Hou:** Supervision, Methodology, Conceptualization. **Yingze Zhang:** Validation, Supervision, Methodology. **Haobo Pan:** Project administration, Methodology, Funding acquisition, Conceptualization. **Xu Cui:** Writing – review & editing, Supervision, Project administration, Methodology, Funding acquisition, Formal analysis, Conceptualization. **Wei Chen:** Writing – review & editing, Validation, Supervision, Resources, Project administration, Methodology, Funding acquisition, Conceptualization.

Ethics approval and consent to participate

All animal experiments have been approved by the Animal Ethics Committee of Shenzhen Institute of Advanced Technology, Chinese Academy of Sciences (Approval number: YSY-DWLL-2021016), and carried out in accordance with the National Laboratory Animal Care and Use Guide.

Declaration of competing interest

Haobo Pan is an editorial board member for Bioactive Materials and was not involved in the editorial review or the decision to publish this article. Hao Zhang, Chunyu Liu, Haobo Pan and Xu Cui are currently employed by Shenzhen Healthemes Biotechnology Co., Ltd. All authors declare that there are no competing interests.

Acknowledgements

This work was supported by the National Key R&D Program of China (Grant No. 2023YFC2416900), the National Natural Science Foundation of China (Grant No. U22A20357, 52072398, 82102584 and 32161160327), Shenzhen Science and Technology Program (Grant No. JCYJ20230807140714030, JCYJ20220818101613028, and JSGGKQTD20210831174330015), and Shenzhen Medical Research Found (B2302031).

Appendix A. Supplementary data

Supplementary data to this article can be found online at https://doi.org/10.1016/j.bioactmat.2024.10.009.

References

[1] E.A. Masters, R.P. Trombetta, K.L. de Mesy Bentley, et al., Evolving concepts in bone infection: redefining "biofilm", "acute vs. chronic osteomyelitis", "the immune proteome" and "local antibiotic therapy", Bone Res. 7 (2019) 20, https://doi.org/10.1038/s41413-019-0061-z.

[2] E.A. Masters, B.F. Ricciardi, K.L.M. Bentley, et al., Skeletal infections: microbial pathogenesis, immunity and clinical management, Nat. Rev. Microbiol. 20 (7) (2022) 385–400, https://doi.org/10.1038/s41579-022-00686-0.

[3] T.F. Moriarty, W.J. Metsemakers, M. Morgenstern, et al., Fracture-related infection, Nat. Rev. Dis. Prim. 8 (1) (2022) 67, https://doi.org/10.1038/s41572-022-00396-0.

[4] J. Peng, Y. Ren, W. He, et al., Epidemiological, clinical and microbiological characteristics of patients with post-traumatic osteomyelitis of limb fractures in southwest China: a hospital-based study, J. Bone Joint Infect. 2 (3) (2017) 149–153, https://doi.org/10.7150/jbji.20002.

[5] Y. Ren, L. Liu, D. Sun, et al., Epidemiological updates of post-traumatic related limb osteomyelitis in China: a 10 years multicentre cohort study, Int. J. Surg. 109 (9) (2023) 2721–2731, https://doi.org/10.1097/JS9.0000000000000502.

[6] P. Kong, Y. Ren, J. Yang, et al., Relapsed boyhood tibia polymicrobial osteomyelitis linked to dermatophytosis: a case report, BMC Surg. 22 (1) (2022) 156, https://doi.org/10.1186/s12893-022-01600-4.

[7] G. Granata, E. Petersen, A. Capone, et al., The impact of armed conflict on the development and global spread of antibiotic resistance: a systematic review, Clin.

Microbiol. Infection : Offic. Pub. Europ. Soci. Clinic. Microbiol. Infect. Diseas. 30 (7) (2024) 858–865, https://doi.org/10.1016/j.cmi.2024.03.029.
[8] F. Ghasemi, A. Jahani, A. Moradi, et al., Different modification methods of poly methyl methacrylate (PMMA) bone cement for orthopedic surgery applications, Archiv. Bone Joint Surg. 11 (8) (2023) 485–492, https://doi.org/10.22038/ABJS.2023.71289.3330.
[9] S. Sebastian, Y. Liu, R. Christensen, et al., Antibiotic containing bone cement in prevention of hip and knee prosthetic joint infections: a systematic review and meta-analysis, J. Orthopaedic Translat. 23 (2020) 53–60, https://doi.org/10.1016/j.jot.2020.04.005.
[10] E.M. Schwarz, A.C. McLaren, T.P. Sculco, et al., Adjuvant antibiotic-loaded bone cement: concerns with current use and research to make it work, J. Orthop. Res. : Offic. Pub. Orthopaedic Res. Soci. 39 (2) (2021) 227–239, https://doi.org/10.1002/jor.24616.
[11] I. Pountos, T. Georgouli, H. Bird, et al., The effect of antibiotics on bone healing: current evidence, Expet Opin. Drug Saf. 10 (6) (2011) 935–945, https://doi.org/10.1517/14740338.2011.589833.
[12] G. Lewis, Antibiotic-free antimicrobial poly (methyl methacrylate) bone cements: a state-of-the-art review, World J. Orthoped. 13 (4) (2022) 339–353, https://doi.org/10.5312/wjo.v13.i4.339.
[13] S.M. Schrader, J. Vaubourgeix, C. Nathan, Biology of antimicrobial resistance and approaches to combat it, Sci. Transl. Med. 12 (549) (2020) eaaz6992, https://doi.org/10.1126/scitranslmed.aaz6992.
[14] J. Ma, L. Zhang, B. Lei, Multifunctional MXene-based bioactive materials for integrated regeneration therapy, ACS Nano 17 (20) (2023) 19526–19549, https://doi.org/10.1021/acsnano.3c01913.
[15] M. Vallet-Regí, D. Lozano, B. González, et al., Biomaterials against bone infection, Adv. Healthcare Mater. 9 (13) (2020) e2000310, https://doi.org/10.1002/adhm.202000310.
[16] S. Gupta, S. Majumdar, S. Krishnamurthy, Bioactive glass: a multifunctional delivery system, J. Contr. Release : Offic. J. Controll. Release Soci. 335 (2021) 481–497, https://doi.org/10.1016/j.jconrel.2021.05.043.
[17] C.L. Romanò, N. Logoluso, E. Meani, et al., A comparative study of the use of bioactive glass S53P4 and antibiotic-loaded calcium-based bone substitutes in the treatment of chronic osteomyelitis: a retrospective comparative study, Bone Joint J. 96-B (6) (2014) 845–850, https://doi.org/10.1302/0301-620X.96B6.33014.
[18] L. Drago, C. Vassena, S. Fenu, et al., In vitro antibiofilm activity of bioactive glass S53P4, Future Microbiol. 9 (5) (2014) 593–601, https://doi.org/10.2217/fmb.14.20.
[19] D.C. Coraça-Huber, M. Fille, J. Hausdorfer, et al., Efficacy of antibacterial bioactive glass S53P4 against *S. aureus* biofilms grown on titanium discs in vitro, J. Orthop. Res. : Offic. Pub. Orthopaedic Res. Soci. 32 (1) (2014) 175–177, https://doi.org/10.1002/jor.22463.
[20] J.T. Silvola, Mastoidectomy cavity obliteration with bioactive glass: a pilot study, Otolaryngol. Head Neck Surg. : Offic. J. Am. Acad. Otolaryngol.-Head Neck Surg. 147 (1) (2012) 119–126, https://doi.org/10.1177/0194599812438168.
[21] J.C. Aurégan, T. Bégué, Bioactive glass for long bone infection: a systematic review, Injury 46 (Suppl 8) (2015) S3–S7, https://doi.org/10.1016/S0020-1383(15)30048-6.
[22] L. Drago, E. De Vecchi, M. Bortolin, et al., Antimicrobial activity and resistance selection of different bioglass S53P4 formulations against multidrug resistant strains, Future Microbiol. 10 (8) (2015) 1293–1299, https://doi.org/10.2217/FMB.15.57.
[23] P. Zhou, B.L. Garcia, G.A. Kotsakis, Comparison of antibacterial and antibiofilm activity of bioactive glass compounds S53P4 and 45S5, BMC Microbiol. 22 (1) (2022) 212, https://doi.org/10.1186/s12866-022-02617-8.
[24] W. Huang, D.E. Day, K. Kittiratanapiboon, et al., Kinetics and mechanisms of the conversion of silicate (45S5), borate, and borosilicate glasses to hydroxyapatite in dilute phosphate solutions, J. Mater. Sci. Mater. Med. 17 (7) (2006) 583–596, https://doi.org/10.1007/s10856-006-9220-z.
[25] N. Stone-Weiss, E.M. Pierce, R.E. Youngman, et al., Understanding the structural drivers governing glass-water interactions in borosilicate based model bioactive glasses, Acta Biomater. 65 (2018) 436–449, https://doi.org/10.1016/j.actbio.2017.11.006.
[26] M.N. Rahaman, B.S. Bal, W. Huang, Review: emerging developments in the use of bioactive glasses for treating infected prosthetic joints, Mater. Sci. Eng., C 41 (2014) 224–231, https://doi.org/10.1016/j.msec.2014.04.055.
[27] H. Zhang, Y. Cui, X. Zhuo, et al., Biological fixation of bioactive bone cement in vertebroplasty: the first clinical investigation of borosilicate glass (BSG) reinforced PMMA bone cement, ACS Appl. Mater. Interfaces 14 (46) (2022) 51711–51727, https://doi.org/10.1021/acsami.2c15250.
[28] A.F. Chen, J. Parvizi, Antibiotic-loaded bone cement and periprosthetic joint infection, J. Long Term Eff. Med. Implants 24 (2–3) (2014) 89–97, https://doi.org/10.1615/jlongtermeffmedimplants.2013010238.
[29] T. Kokubo, H. Takadama, How useful is SBF in predicting in vivo bone bioactivity? Biomaterials 27 (15) (2006) 2907–2915, https://doi.org/10.1016/j.biomaterials.2006.01.017.
[30] J. Bingham, When and how should I use antibiotic cement in primary and revision joint arthroplasty? J. Arthroplasty 37 (8) (2022) 1435–1437, https://doi.org/10.1016/j.arth.2022.02.001.
[31] C. Paul, E. Steinhauser, K.D. Kühn, Verarbeitungseigenschaften und Viskositäten von PMMA-Knochenzementen [Processing properties and viscosities of PMMA bone cements], Orthopadie (Heidelberg, Germany) 52 (12) (2023) 957–967, https://doi.org/10.1007/s00132-023-04450-x.
[32] A.C. Matos, C.F. Marques, R.V. Pinto, et al., Novel doped calcium phosphate-PMMA bone cement composites as levofloxacin delivery systems, Int. J. Pharm. 490 (1–2) (2015) 200–208, https://doi.org/10.1016/j.ijpharm.2015.05.038.
[33] W. Jun, K. Yi-Jun, C. Fei, et al., Application of an antibiotic crescent-shaped polymethylmethacrylate strut in thoracic vertebral tuberculosis, Turkish Neurosurg. 23 (1) (2013) 107–112, https://doi.org/10.5137/1019-5149.JTN.4218-11.0.
[34] W. Xiu, L. Wan, K. Yang, et al., Potentiating hypoxic microenvironment for antibiotic activation by photodynamic therapy to combat bacterial biofilm infections, Nat. Commun. 13 (1) (2022) 3875, https://doi.org/10.1038/s41467-022-31479-x.
[35] X. Li, Y. Liu, X. Qi, et al., Sensitive activatable nanoprobes for real-time ratiometric magnetic resonance imaging of reactive oxygen species and ameliorating inflammation in vivo, Advanced materials (Deerfield Beach, Fla.) 34 (19) (2022) e2109004, https://doi.org/10.1002/adma.202109004.
[36] M. Peacock, Phosphate metabolism in health and disease, Calcif. Tissue Int. 108 (1) (2021) 3–15, https://doi.org/10.1007/s00223-020-00686-3.
[37] D. Ma, R.M.Q. Shanks, C.M. Davis, et al., Viable bacteria persist on antibiotic spacers following two-stage revision for periprosthetic joint infection, J. Orthop. Res. : Offic. Pub. Orthopaedic Res. Soci. 36 (1) (2018) 452–458, https://doi.org/10.1002/jor.23611.
[38] A.M. VanHook, Antibiotic-induced inflammation, Sci. Signal. 15 (745) (2022) eade1683, https://doi.org/10.1126/scisignal.ade1683.
[39] J. Davies, B.D. Davis, Misreading of ribonucleic acid code words induced by aminoglycoside antibiotics. The effect of drug concentration, J. Biol. Chem. 243 (12) (1968) 3312–3316.
[40] A.N. Brown, M.T. Anderson, M.A. Bachman, et al., The ArcAB two-component system: function in metabolism, redox control, and infection, Microbiol. Mol. Biol. Rev. : MMBR 86 (2) (2022) e0011021, https://doi.org/10.1128/mmbr.00110-21.
[41] S. Józefowski, M. Czerkies, A. Łukasik, et al., Ceramide and ceramide 1-phosphate are negative regulators of TNF-α production induced by lipopolysaccharide, Journal of immunology (Baltimore, Md. : 1950) 185 (11) (2010) 6960–6973, https://doi.org/10.4049/jimmunol.0902926.
[42] T. Serizawa, S. Yamaguchi, K. Sugiura, et al., Antibacterial synthetic nanocelluloses synergizing with a metal-chelating agent, ACS Appl. Bio Mater. 7 (1) (2024) 246–255, https://doi.org/10.1021/acsabm.3c00846.
[43] J. Tan, D. Wang, H. Cao, et al., Effect of local alkaline microenvironment on the behaviors of bacteria and osteogenic cells, ACS Appl. Mater. Interfaces 10 (49) (2018) 42018–42029, https://doi.org/10.1021/acsami.8b15724.
[44] C.J. Sanchez, C. L. Jr Ward, D.R. Romano, et al., Staphylococcus aureus biofilms decrease osteoblast viability, inhibits osteogenic differentiation, and increases bone resorption in vitro, BMC Muscoskel. Disord. 14 (2013) 187, https://doi.org/10.1186/1471-2474-14-187.
[45] M.H. Saier Jr., The bacterial phosphotransferase system: new frontiers 50 Years after its discovery, J. Mol. Microbiol. Biotechnol. 25 (2–3) (2015) 73–78, https://doi.org/10.1159/000381215.
[46] F.L. Theodoulou, I.D. Kerr, ABC transporter research: going strong 40 years on, Biochem. Soc. Trans. 43 (5) (2015) 1033–1040, https://doi.org/10.1042/BST20150139.
[47] M.E. Bosch, B.P. Bertrand, C.E. Heim, et al., Staphylococcus aureus ATP synthase promotes biofilm persistence by influencing innate immunity, mBio 11 (5) (2020), https://doi.org/10.1128/mBio.01581-20.
[48] K.L. Painter, A. Hall, K.P. Ha, et al., The electron transport chain sensitizes Staphylococcus aureus and Enterococcus faecalis to the oxidative burst, Infect. Immun. 85 (12) (2017), https://doi.org/10.1128/IAI.00659-17.
[49] S. M, R.P. N, S. Rajendrasozhan, Bacterial redox response factors in the management of environmental oxidative stress, World J. Microbiol. Biotechnol. 39 (1) (2022) 11, https://doi.org/10.1007/s11274-022-03456-5.
[50] Z. Lyu, S. Ding, D. Du, et al., Recent advances in biomedical applications of 2D nanomaterials with peroxidase-like properties, Adv. Drug Deliv. Rev. 185 (2022) 114269, https://doi.org/10.1016/j.addr.2022.114269.
[51] W. Stahl, H. Sies, Antioxidant activity of carotenoids, Mol. Aspect. Med. 24 (6) (2003) 345–351, https://doi.org/10.1016/s0098-2997(03)00030-x.
[52] A.M. Stock, V.L. Robinson, P.N. Goudreau, Two-component signal transduction, Annu. Rev. Biochem. 69 (2000) 183–215, https://doi.org/10.1146/annurev.biochem.69.1.183.
[53] Y. Xue, L. Zhang, F. Liu, et al., Alkaline "nanoswords" coordinate ferroptosis-like bacterial death for antibiosis and osseointegration, ACS Nano 17 (3) (2023) 2711–2724, https://doi.org/10.1021/acsnano.2c10960.
[54] J. Fu, W. Zhu, X. Liu, et al., Self-activating anti-infection implant, Nat. Commun. 12 (1) (2021) 6907, https://doi.org/10.1038/s41467-021-27217-4.
[55] D.A. Robinson, J.E. Bechtold, C.S. Carlson, et al., Development of a fracture osteomyelitis model in the rat femur, J. Orthop. Res. : Offic. Pub. Orthopaedic Res. Soci. 29 (1) (2011) 131–137, https://doi.org/10.1002/jor.21188.
[56] K. Wannfors, L. Hammarström, Infectious foci in chronic osteomyelitis of the jaws, Int. J. Oral Surg. 14 (6) (1985) 493–503, https://doi.org/10.1016/s0300-9785(85)80055-7.
[57] L.B. Engesaeter, S.A. Lie, B. Espehaug, et al., Antibiotic prophylaxis in total hip arthroplasty: effects of antibiotic prophylaxis systemically and in bone cement on the revision rate of 22,170 primary hip replacements followed 0-14 years in the Norwegian Arthroplasty Register, Acta Orthop. Scand. 74 (6) (2003) 644–651, https://doi.org/10.1080/00016470310018135.
[58] W.R. Wang, J. Li, J.T. Gu, et al., Optimization of lactoferrin-derived amyloid coating for enhancing soft tissue seal and antibacterial activity of titanium implants, Adv. Healthcare Mater. 12 (11) (2023) e2203086, https://doi.org/10.1002/adhm.202203086.

[59] L. Li, Y. Yin, S. Zhang, et al., BMEMat (2024) e12081, https://doi.org/10.1002/bmm2.12081.
[60] W. Niu, Y. Guo, Y. Xue, et al., Monodisperse branched molybdenum-based bioactive nanoparticles significantly promote osteogenic differentiation of adipose-derived stem cells, Part. Part. Syst. Char. 36 (2019) 1900105, https://doi.org/10.1002/ppsc.201900105.
[61] F. Baino, S. Hamzehlou, S. Kargozar, Bioactive glasses: where are we and where are we going? J. Funct. Biomater. 9 (1) (2018) 25, https://doi.org/10.3390/jfb9010025.
[62] Y. Xue, W. Niu, M. Wang, et al., Engineering a biodegradable multifunctional antibacterial bioactive nanosystem for enhancing tumor photothermo-chemotherapy and bone regeneration, ACS Nano 14 (1) (2020) 442–453, https://doi.org/10.1021/acsnano.9b06145.
[63] M.T. Cunha, M.A. Murça, S. Nigro, et al., In vitro antibacterial activity of bioactive glass S53P4 on multiresistant pathogens causing osteomyelitis and prosthetic joint infection, BMC Infect. Dis. 18 (1) (2018) 157, https://doi.org/10.1186/s12879-018-3069-x.
[64] J. Zhang, V. Boyes, F. Festy, et al., In-vitro subsurface remineralisation of artificial enamel white spot lesions pre-treated with chitosan, Dent. Mater. 34 (8) (2018) 1154–1167, https://doi.org/10.1016/j.dental.2018.04.010.
[65] W. Zhang, F. Zhao, D. Huang, et al., Strontium-substituted submicrometer bioactive glasses modulate macrophage responses for improved bone regeneration, ACS Appl. Mater. Interfaces 8 (45) (2016) 30747–30758, https://doi.org/10.1021/acsami.6b10378.
[66] N.C. Lindfors, P. Hyvönen, M. Nyyssönen, et al., Bioactive glass S53P4 as bone graft substitute in treatment of osteomyelitis, Bone 47 (2) (2010) 212–218, https://doi.org/10.1016/j.bone.2010.05.030.
[67] T.A. Malat, M. Glombitza, J. Dahmen, et al., The use of bioactive glass S53P4 as bone graft substitute in the treatment of chronic osteomyelitis and infected non-unions - a retrospective study of 50 patients, Z. für Orthop. Unfallchirurgie 156 (2) (2018) 152–159, https://doi.org/10.1055/s-0043-124377.
[68] M. Bigoni, M. Turati, N. Zanchi, et al., Clinical applications of Bioactive glass S53P4 in bone infections: a systematic review, Eur. Rev. Med. Pharmacol. Sci. 23 (2 Suppl) (2019) 240–251, https://doi.org/10.26355/eurrev_201904_17498.
[69] M. Gonzalez Moreno, M.E. Butini, E.M. Maiolo, et al., Antimicrobial activity of bioactive glass S53P4 against representative microorganisms causing osteomyelitis - real-time assessment by isothermal microcalorimetry, Colloids Surf. B Biointerfaces 189 (2020) 110853, https://doi.org/10.1016/j.colsurfb.2020.110853.
[70] D.M. Marques, V.C. Oliveira, M.T. Souza, et al., Biomaterials for orthopedics: anti-biofilm activity of a new bioactive glass coating on titanium implants, Biofouling 36 (2) (2020) 234–244, https://doi.org/10.1080/08927014.2020.1755842.
[71] B. Wang, Y. Wang, J. Zhang, et al., ROS-induced lipid peroxidation modulates cell death outcome: mechanisms behind apoptosis, autophagy, and ferroptosis, Arch. Toxicol. 97 (6) (2023) 1439–1451, https://doi.org/10.1007/s00204-023-03476-6.